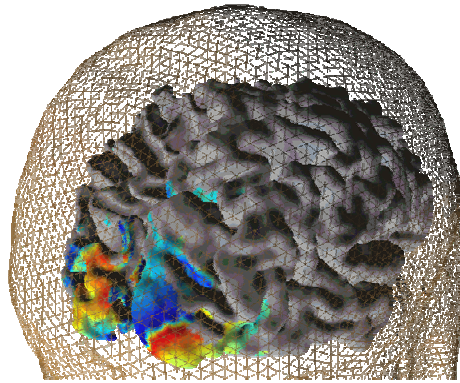


MASTER OF SCIENCE THESIS

Human Visual Cortex

-O-

Investigations using fMRI



Supervisor: Lars Kai Hansen

Kristoffer Hougaard Madsen

s991489

May 2004

Intelligent Signal Processing Group
Department of Informatics and Mathematical Modelling
Technical University of Denmark

Danish Research Centre for Magnetic Resonance
Copenhagen University Hospital, Hvidovre



Preface

The present study is a master thesis in engineering at the Technical University of Denmark (DTU). The project is a collaboration between the intelligent signal processing group, department of Informatics Mathematics and Modelling (IMM), DTU and the Danish Research Centre for Magnetic Resonance (DRCMR), Copenhagen University Hospital, Hvidovre.

The principal supervisor of the project is Professor Lars Kai Hansen, IMM, DTU. The co-supervisor is PhD student Torben Ellegaard Lund, DRCMR.

The present thesis summarizes part of the experiments carried out at DRCMR during the project period, which would not have been possible without the warm welcome and help from the staff at DRCMR. A special thanks to Torben Ellegaard Lund is appropriate for being more helpful than could be expected in planning, implementation, guidance and countless discussions during the project.

Professor dr. phil. Axel Larsen, department of psychology, University of Copenhagen (KU) is also acknowledged for the help in planning the psychological basis of the experiments and for providing the experiment described in section 4.3.

Also Per Skaftø Hansen, Danish Bankers' Association is acknowledged for providing images used in the stereovision paradigm described in section 4.2.

Special thanks are directed to friends, co-workers and family for help and guidance throughout the project period, especially during the last phase of the project for reading through the draft manuscript.

Last but not least special thanks go to the anonymous subjects for participation, concentration, patience, tolerance and “not moving too much” during the occasionally boring and exhausting data acquisition.

Kristoffer Madsen

Abstract

The present work describes a method for investigation of the visual cortex in humans using functional magnetic resonance imaging (fMRI). A method for analysis of retinotopic mapping data using a general linear model is suggested and a method for determining the hemodynamic lag based on the measurement is described. The hemodynamic lag in the visual cortex is found to be 4.2 s. Also a method for performing perimetry (visual field testing) using fMRI is suggested, indicating interesting perspectives for further investigations of clinically relevant patients.

Furthermore, the project presents two additional studies of the human visual cortex. The first study aims to investigate stereovision by the use of colour coded 3 dimensional images whereas the second experiment explores connections between the primary visual cortex (V1) and V5 (MT). The results showed a possible activation of V3 and other secondary visual areas in response to stereo stimuli. Preliminary results indicating proof of V5 to V1 back projection is presented.

In addition the retinotopic mapping described has been planned for clinically investigations of patients with Optic Neuritis.

Dansk resumé

Dette projekt beskriver en metode til undersøgelse af synsbarken hos mennesker ved brug af funktionel magnetisk resonans billeddannelse. Projektet foreslår en metode til analyse af data til retinotopisk kortlægning af synsbarken i en generel lineær model. Ved brug af ovenstående præsenteres også en metode til at estimere forsinkelsen af det hæmodynamiske respons på neural aktivitet en forsinkelse på 4.2 s blev fundet. Yderligere foreslås en metode til udførelse af perimetri (undersøgelse af synsudfald) vha. fMRI.

Yderligere præsenteres to undersøgelser af den visuelle synsbark. Det ene er et studie til kortlægning af stereosyn ved brug af farvekodede stereobilleder. Det andet studie har til formål at undersøge forbindelser mellem synsområderne V1 og V5 (MT). I forbindelse med undersøgelsen af stereosyn præsenteres præliminære resultater som indikerer aktivitet i sekundære visuelle områder herunder V3. Ligeledes præsenteres foreløbige resultater som indikerer tilstedeværelsen af forbindelser fra V5 til V1.

Resultater fra studiet omhandlende retinotopisk kortlægning har givet anledning til planlægning af en klinisk undersøgelse af patienter med sygdommen Opticus Neuritis.

Abbreviations

3-D	3 Dimensional
AU	Arbitrary Units
BA	Brodmann Area
BOLD	Blood Oxygenation Level Dependent
CBF	Cerebral Blood Flow
CBV	Cerebral Blood Volume
CCW	Counter-ClockWise
CMRO ₂	Cerebral Metabolic Ratio of O ₂
COR	Coronal
CS	Calcarine Sulcus
CSF	Cerebrospinal Spinal Fluid
CW	ClockWise
EOI	Effects Of Interest
EPI	Echo-Planar Imaging
FA	Flip Angle
FDR	False Discovery Rate
FEW	Family-Wise Error
FFT	Fast Fourier Transform
fMRI	functional Magnetic Resonance Imaging
FOV	Field of View
GE	Gradient Echo
GLM	General Linear Model
GM	Grey Matter
HRF	Hemodynamic Response Function
LGN	Lateral Geniculate Nucleus
MPRAGE	Magnetisation Prepared Rapid Gradient Echo
MRI	Magnetic Resonance Imaging
SAG	Sagittal
SNR	Signal to Noise Ratio
SPM	Statistical Parametric Map
T ₁	Longitudinal relaxation time
T ₂	Transversal relaxation time
T ₂ *	Transversal relaxation time in presence of field inhomogeneity
TE	Echo Time
TR	Repetition Time
TRA	Transversal
WM	White Matter

Table of Contents

1	Introduction	1
1.1	Overview	2
2	Brain and Vision	3
2.1	The Brain: An Overview	4
2.2	Visual Pathways	5
2.2.1	Retina	5
2.2.2	Lateral Geniculate Nucleus	7
2.3	Visual Cortex	8
2.3.1	Primary Visual Cortex	8
2.3.2	Secondary Visual Cortices	9
2.3.3	Cortical Magnification	9
2.3.4	Retinotopic Organization	10
2.4	Blood Oxygenation Level Dependent Signal	11
3	Methods	13
3.1	Hypothesis Driven Methods	13
3.1.1	Linear Cross Correlation Analysis	13
3.1.2	General Linear Model	14
3.1.3	Correction for Serial Correlations	15
3.1.4	Inferences in the GLM	17
3.2	Data Driven Methods	18
3.2.1	Independent Component Analysis	18
3.3	Noise	19
3.4	Pre-processing Functional Data	21
3.4.1	Motion Correction	21
3.4.2	High Pass Filtering	23
3.4.3	Slice Time Correction	23
3.4.4	Smoothing	24
3.5	Processing Anatomical Data	24
3.5.1	Normalization	25
3.5.2	Inhomogeneity Correction	25
3.5.3	Segmentation	27
3.5.4	Inflation	28
3.5.5	Unfolding	29
3.5.6	Distortion Correction	29
3.5.7	Physiological Noise	30
4	Experiments	33
4.1	Retinotopic Mapping	33
4.1.1	Experimental Setup	34
4.1.2	Visual Stimuli	35
4.1.3	Scanning protocol	38
4.1.4	Data Analysis	39
4.1.5	Results	44

4.2	Stereo Vision	55
4.2.1	Experimental Setup and Data Acquisition	55
4.2.2	Visual Stimuli	55
4.2.3	Data Acquisition	57
4.2.4	Data Analysis	57
4.2.5	Results.....	57
4.3	V5-V1 Back Projection	60
4.3.1	Experimental Setup.....	60
4.3.2	Visual Stimuli	60
4.3.3	Data Analysis	61
4.3.4	Results.....	61
4.4	Other Results	63
4.4.1	Physiological Noise and Serial Correlation	63
4.4.2	Retinotopic Mapping and Robustness	65
5	Discussion.....	67
	Conclusion	71
	Bibliography.....	73

1 Introduction

Several scientific reasons exist for investigation of the human brain. The function of the brain is complicated and we usually rely on indirect measures to determine neural activity (such as blood flow). Consequently neither measurements nor modelling of brain functions are easy tasks.

Only a decade has past since Functional Magnetic Resonance Imaging (fMRI) was introduced [59,60] and already this method is one of the most promising and intensively used in the investigation of the human brain.

The traditionally MRI method is widely used in providing anatomical information and serves as a diagnostic tool for various diseases. The current research in fMRI extends the MRI method to provide additional information that could serve as an important tool in pathology as well as in basic function of various physiological processes, for example the visual pathways.

fMRI in combination with retinotropic mapping stimuli and cortical surface reconstruction have made it possible to define the borders of early visual areas in primates as well as in humans [21,68,90]. However, when concerning the higher visual areas these methods have so far proven less useful and many functions of the visual areas in humans are yet to be defined precisely.

The fMRI analysis depends on the Blood Oxygenation Level Dependent (BOLD) contrast. This measure of activity is based on the assumption that increased neuronal activity gives rise to localized increased blood flow [59,60]. One of the most challenging aspects of fMRI is the extraction of the BOLD signal from the MR signal. Various noise sources contribute to the complexity of this signal as for example respiration, cardiac noise, instability in hardware etc. In order to remove at least some of these confounders, pre-processing of the functional data is necessary, thus altering the data before the actual statistical analysis. The pre-processing steps are followed by statistical analysis, where the general linear model (GLM) method first implemented by Friston et al. is widely accepted [28].

The present study aims to investigate the human visual cortex using BOLD fMRI. In order to accomplish this, various analysis methods and visualization techniques will be utilized. The data obtained during this study was analysed using the Brain-Voyager QX 1.0 software, however, when insufficient or not yet implemented self-written routines was often necessary.

1.1 Overview

Chapter 2 serves as a brief and simple introduction to brain and vision including a brief introduction to the signal measured with fMRI. As a full description of fMRI is well beyond the scope of this text, no description of fMRI in general is provided. Readers not familiar with the subject should refer to the literature for more information. A good introduction to fMRI is given by Buxton [10] whereas a more detailed description of the echo-planar imaging (EPI) technique can be found in [66].

Chapter 3 gives a relatively comprehensive description of the methods used in this study. Most (but not all) of these methods are standard in fMRI.

Chapter 4 is the most important part of this work, as it describes the experiments performed in this study and presents the results. The chapter is divided into sections according to the experiments. Each experiment is divided into subsections describing the experimental setup and the data analysis followed by a presentation and short discussion of the results.

Chapter 5 provides a discussion of the results obtained and suggests improvements and further work.

Additional information, source code etc. is provided on the web page:
www.student.dtu.dk/~s991489/thesis/

2

Brain and Vision

This chapter provides a very short introduction to the human brain in the context of visual stimuli processing. Quite a large part of the human brain is dedicated to processing of visual stimuli suggesting that vision has been evolutionary very important. A lot of effort has been done to examine the human visual system implying that the function is quite well understood as compared to other parts of the brain.

The sections 2.2 and 2.3 are largely, unless otherwise stated, inspired by Hubel [41] and Zeki [103] who have both been pioneers in the context of brain and vision.

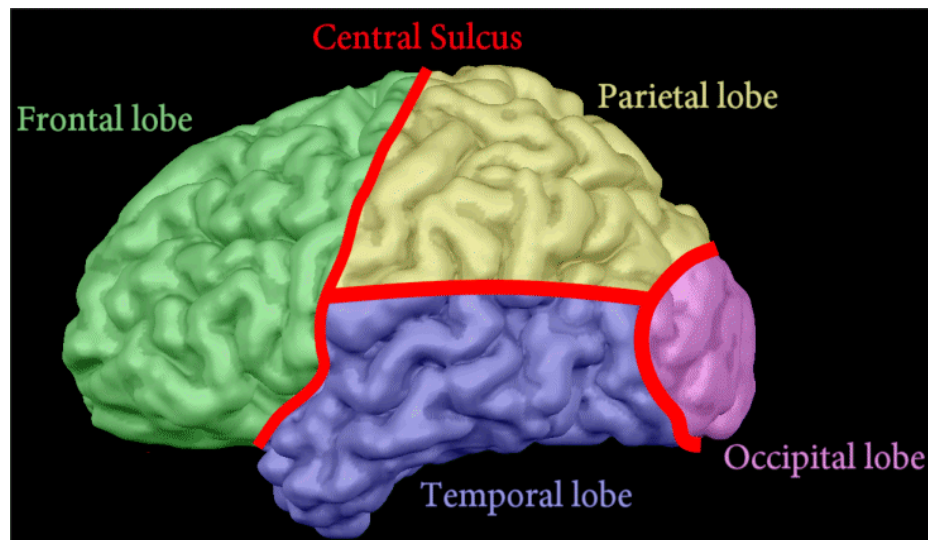


Figure 2.1: Lobes in the cerebral cortex. The figure is a reconstruction of the left GM surface from one of the subjects used in the study. The different lobes have been roughly sketched and coloured. Gyri (singular gyrus) are the outwards folds in the brain tissue, whereas areas with negative curvature (inwards folds - dark) are in general called sulci (singular sulcus). Very deep sulci, such as the division between the hemispheres, are denoted fissures.

2.1 The Brain: An Overview

Roughly the brain consists of white matter (myelinated axons) surrounded by grey matter (cell bodies) as can be seen in figure 2.2.

Figure 2.1 shows how the cerebral cortex is divided into lobes. In this study the most interesting part is the occipital lobe in the posterior region as it is related to visual processing.

Visualization of the brain is possible using isometric slices. Radiological convention is commonly used to show isometric planes meaning that the left part of the brain is shown to the right and vice versa. The opposite (left=left, right=right) is known as neurological convention. In this study figures will be shown in radiological convention unless otherwise stated; this convention does not apply to 3-D figures.

A vertical plane cut parallel to the ears is denoted a sagittal plane, whereas a plane parallel to the face is a coronal plane. Finally a horizontal plane is a transversal plane, 3D views of these cuts are illustrated in figure 2.3.

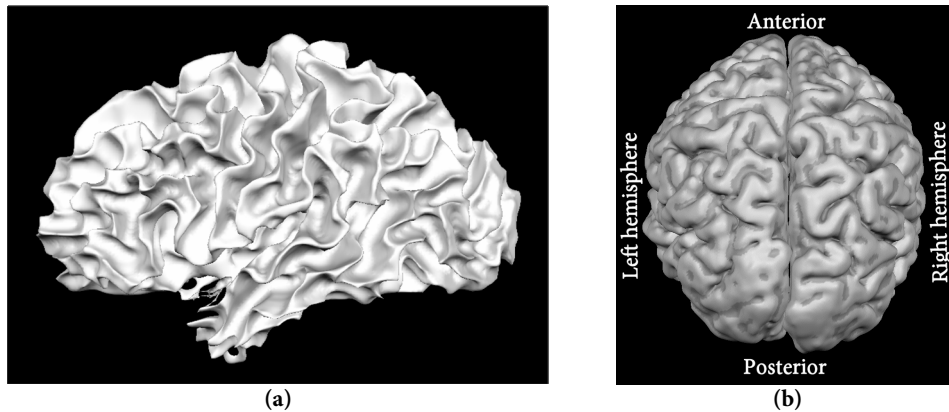


Figure 2.2: WM/GM and hemispheres.

(a) shows a reconstruction of the WM surface in one of the subjects and (b) shows the GM surrounding it. Because the figures are 3D views radiological convention is not used.

Anterior represents frontal areas whereas posterior designates parts to the back. Inferior refer to bottom while superior refers to the top. Again medial refers to near the thalamus in the midbrain (division between hemispheres). Dorsal/ventral refers to over/below.

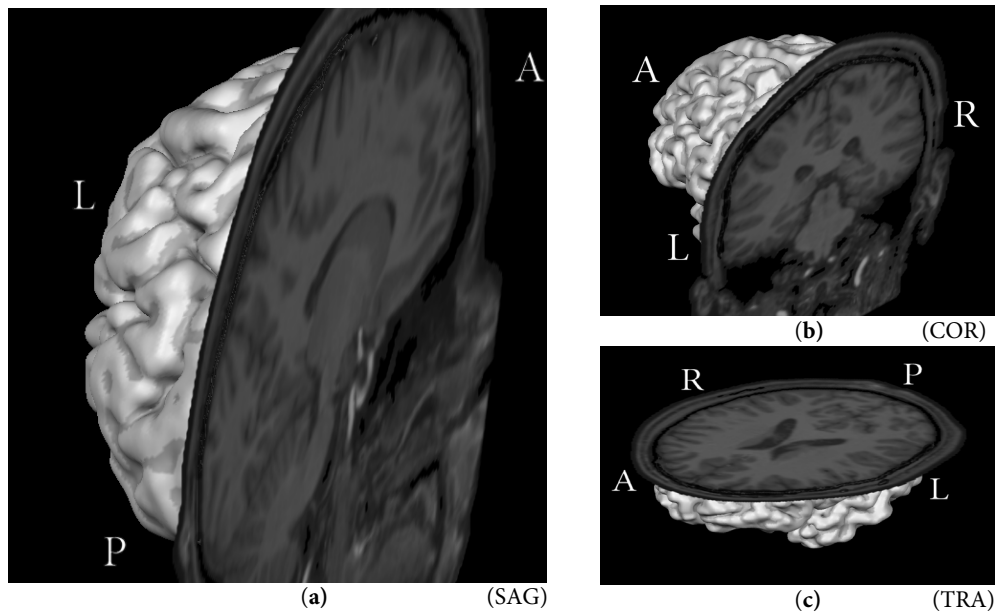


Figure 2.3: Isometric plane projections in the brain.

Figure (a): sagittal plane, figure (b): coronal plane, figure (c): transversal plane

2.2 Visual Pathways

Before visual stimuli arrive in the cortex they must pass through the visual pathway, which will be described in the following sections.

2.2.1 Retina

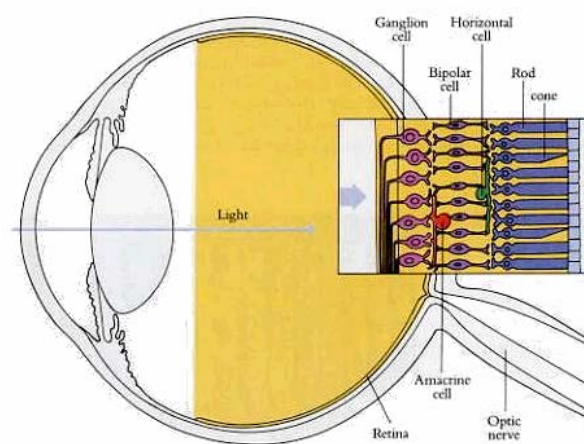
The light from the environment is focused onto the back of the eye by the cornea and the lens¹. In the back of the eyeball 3 layers of cells constitute the retina. The cell layer farthest to the back consists of actual receptors; there are two types of receptors: rods and cones. Cones are responsible for detailed vision and colours but do not respond to dim light, whereas rods respond to dim light and are responsible for more coarse vision.

The middle layer consists of 3 cell types; bipolar-, horizontal- and amacrine cells. The bipolar cells receive input from the receptors and feed the signals into the last layer – the retinal ganglion cells. The two remaining cell types create links running parallel to the retinal layer. Horizontal cells link together photoreceptors and bipolar cells while amacrine cells link together retinal ganglion cells and bipolar cells (see figure 2.4).

¹ The image on the retina will appear flipped left-right and upside-down.

In the centre of our visual field (the fovea) cones are most common and the two layers on top are displaced to the sides to create a depression in the retinal surface where light can pass directly into the photoreceptors. The correspondence between the number of photoreceptors and ganglion cells in the fovea is approximately 1:1, however, with increasing distance to the fovea more photoreceptors converge onto a single ganglion cell. The number of retinal ganglion cells is approximately 1 million compared to the 125 million photoreceptors.

The axons from the ganglion cells run along the surface of the retina and converge to leave through the optic nerve. The place where the optic nerve leaves the eye is also known as the blind spot because of the lack of photoreceptors in this area.



Hubel, 1995

Figure 2.4: The eye and the retina, the figure illustrates the eyeball and the retina consisting of 3 cell layers. [41]

2.2.2 Lateral Geniculate Nucleus

When the optic nerves have left each of the eyes, they meet in the optic chiasm. Here they are divided into left and right hemifield and travel through the optic tract to arrive at the Lateral Geniculate Nucleus (LGN). Visual inputs from the left hemifield meet in the right LGN and vice versa. Although most connections pass through the LGN, some direct connections exist to other areas such as the superior colliculus, the suprachiasmatic nucleus and midbrain nuclei. The superior colliculus is responsible for coordinating rapid eye movements and the midbrain nuclei are responsible for related tasks such as adjusting the size of the pupils. The suprachiasmatic nucleus is believed to be related to light and the day-night cycle [65].

The LGN consists of 6 cell layers (see figure 2.5b) divided according to which eye they receive input from. Most of the axons from the LGN are projected onto the primary visual cortex through the optics radiations.

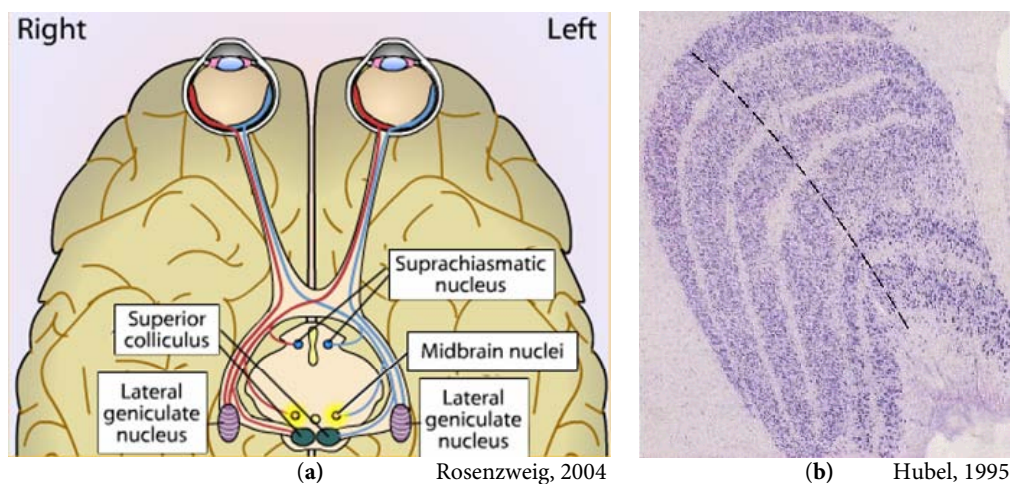


Figure 2.5: Connections to the LGN.

Figure (a) illustrates how the optic tracts connect to the LGN and other nuclei in the thalamus. Red lines show connections from the left hemifield whereas blue conforms to the right hemifield. Note that the image is showed left-right flipped to conform to radiological convention. [65]

Figure (b) shows the 6 layers in the left LGN of the macaque. The section is cut parallel to the face and each stained dot represents one cell. Two adjacent layers in the LGN generally receive information from opposite eyes, however there is one exception to this rule; the correct sequence is (O-S-S-O-S-O-S) where S denotes same side eye and O side opposite eye (starting from the bottom in figure b). [41]

2.3 Visual Cortex

2.3.1 Primary Visual Cortex

The primary visual cortex (V1) is also called the striate cortex due to its striped cytoarchitectural structure. The primary visual cortex is situated along the Calcarine Sulcus (CS) as shown in figure 2.6, the sulcus (inwards fold) separates the upper and lower visual field with the upper visual field being located in the ventral (lower) part and vice versa. The most posterior part of V1 corresponds to the fovea and moving to increasingly anterior parts of V1 is equivalent to moving towards the periphery in the visual field [16]. This point-to-point relationship will be investigated more comprehensively in section 0.

V1 will react on any visual stimuli (is not very specialized); consequently, V1 is heavily interconnected with the more specialized secondary visual cortices by both forward and backward projections. As mentioned earlier visual stimuli are processed in the contralateral side implying that each hemisphere processes stimuli from both eyes. This gives rise to the phenomenon known as ocular dominance columns as adjacent points in the cortex are from opposite sides in the visual field, this is illustrated in figure 2.8. Some cells in V1 are dissipative-sensitive and are therefore believed to be related to stereovision [4].

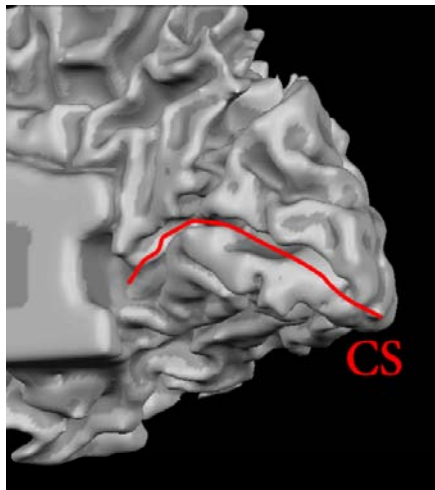


Figure 2.6: Calcarine Sulcus. The figure shows a dilated and smoothed view of the reconstructed GM/WM surface of the left hemisphere, the CS is marked by hand.

2.3.2 Secondary Visual Cortices

Beside the primary visual cortex many secondary areas related to vision have been located in monkeys. However, considerable effort has been made to determine the equivalent areas in humans [64,68,69,80,81,83-85,88,91]. The secondary visual cortices are also called the extrastriate cortex and are related to more complex visual processing. The function of many of the visual areas is not entirely understood, however for some areas there is a strong indication of their basic function. V5 also known as MT+ is related to movement [42], and V3 is believed to be involved in the processing of shape. Zeki [103] and others have suggested that area V4 is specialized for colour processing, but recent evidence [91] challenge this claim

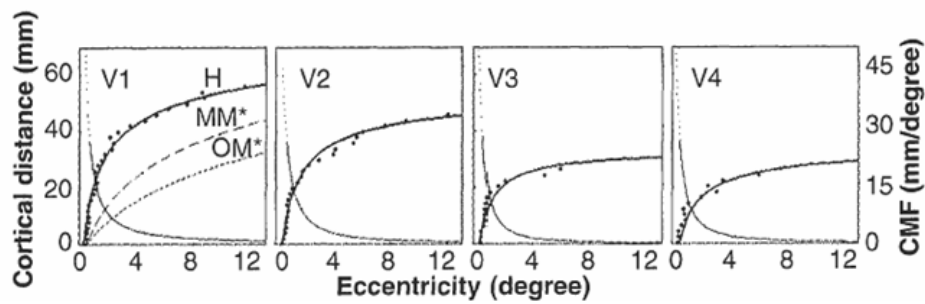
2.3.3 Cortical Magnification

As is expected due to the vast number of ganglion cells near the fovea compared to the periphery, the representation in the cortex is not linear. Physiological studies of the monkey brain have established a connection between distances in the visual field and the corresponding distance in the visual cortex [67].

Equation (2.1) provides the relationship between change in eccentricity ΔE (degrees) and distance in the visual cortex Δx (mm). The ratio depends upon the eccentricity E and the two constants A and E_2 .

$$M(E) = \frac{\Delta x}{\Delta E} = \frac{A}{E + E_2} \quad (2.1)$$

Determination of the constants in humans have been accomplished by several authors [19,21,63,68,72,93]. The cortical magnification (M) also extends to other secondary visual areas [68] as can be seen in figure 2.7.



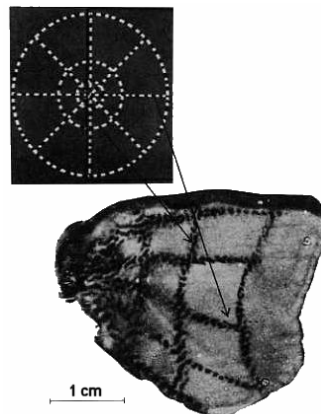
Sereno et al., 1995

Figure 2.7: Cortical magnification in the primate visual cortex. H denotes human, MM* the macaque monkey and OM* the owl monkey. It is seen that the cortical magnification extends to secondary visual areas. Heavy lines refer to the distance in the cortex from the periphery (left scale), the thin lines are the cortical magnification factor (right scale). [68]

2.3.4 Retinotopic Organization

Retinotopic organization is a term that refers to the fact that topological shape from the retina is preserved in the cortex, meaning that adjacent points in the retina will be mapped to adjacent point in the visual cortex. Figure 2.8 illustrates this in the primary visual cortex of the macaque [86]. The point-to-point mapping also exists in other parts of the brain, for example in the somatosensory system.

This preserved geometric shape is most explicit in the primary visual cortex, however retinotopic mapping exists in most parts of the visual cortex.



Totell et al., 1982

Figure 2.8: Retinotopic organization in the macaque striate cortex. Tootell et al. showed this convincing figure in a paper from 1982. The animal was given a tracer before the stimulus shown above was presented monocularly at 3 Hz reversal rate. Finally the animal was dissected and the striate cortex was cut and unfolded as shown in the figure above. The dot pattern in the figure illustrates the ocular dominance columns [86].

2.4 Blood Oxygenation Level Dependent Signal

The signal measured in fMRI is usually the Blood Oxygenation Level Dependent (BOLD) signal. This measure of activity is (as many others) based on the assumption that increased neuronal activity gives rise to localized increased blood flow. BOLD measurements were first performed on rats by Ogawa et al. [59,60] in 1990, and later on humans in 1992 [61].

The measurement of BOLD is based on the Echo-Planar Imaging (EPI) sequence and the actual effect measured is signal loss due to deoxygenated hemoglobin (dHb) (gives rise to field distortion). Oxygenated hemoglobin (Hb) is weakly diamagnetic whereas dHb is weakly paramagnetic. The presence of dHb results in loss of MR signal depending on the concentration of dHb (because of the susceptibility effect).

At first glance increased neuronal activity would be expected to cause increased oxygen consumption thereby decreasing the MR signal. However, the phenomenon is more complicated and in general the BOLD signal is expected to be caused by 3 effects; the cerebral blood flow (CBF), the cerebral blood volume (CBV) and the cerebral metabolic rate of O_2 (CMRO₂). The following description of the BOLD signal is motivated by the model suggested by Buxton et al. [9] also known as the Balloon model.

An increased oxygen extraction due to neuronal activity results in a short increase in the dHb. This should give rise to a short decrease in the MR signal (initial dip), however this has only been seen experimentally in anesthetized cats at very high field strengths [45].

The increased oxygen consumption gives rise to an increased CBF dominating the first effect thus decreasing dHb (increase in MR signal). The large increase in CBF is expected to be necessary because neuronal activity is limited by the blood flow in resting state.

The increase in blood flow expands the blood vessels and increases CBV, thus increasing the amount of dHb. This effect is insignificant compared to the effect of CBF. However, it is expected to cause the post stimulus undershoot because it takes longer for CBV than CBF to return to baseline.

The total temporal extent of the BOLD response is expected to be approximately 30 seconds.

The response to stimuli is normally modelled as a simple convolution² of the stimuli time course with the expected response due to a single activation. Such a model

² Convolution is the process of mixing two functions, it is also known as folding (from German “faltung”). A convolution of two functions (f and g) in an infinite range is given by

the following integral: $f * g = \int_{-\infty}^{\infty} g(\tau)f(t - \tau)d\tau$. In the frequency domain (Fourier) a convolution is a simple multiplication.

is known as a hemodynamic response function (HRF) – an example of this is the SPM2³ canonical HRF shown in figure 2.9. By including time derivatives (or similar) in a general linear model (see section 3.1.2 on page 14) it is possible to model variations in the response (delay and dispersion).

This approach is not able to model the non-linearity (saturation) in the balloon model [9], however to account for this Friston et al. suggests using Volterra kernels⁴ [32].

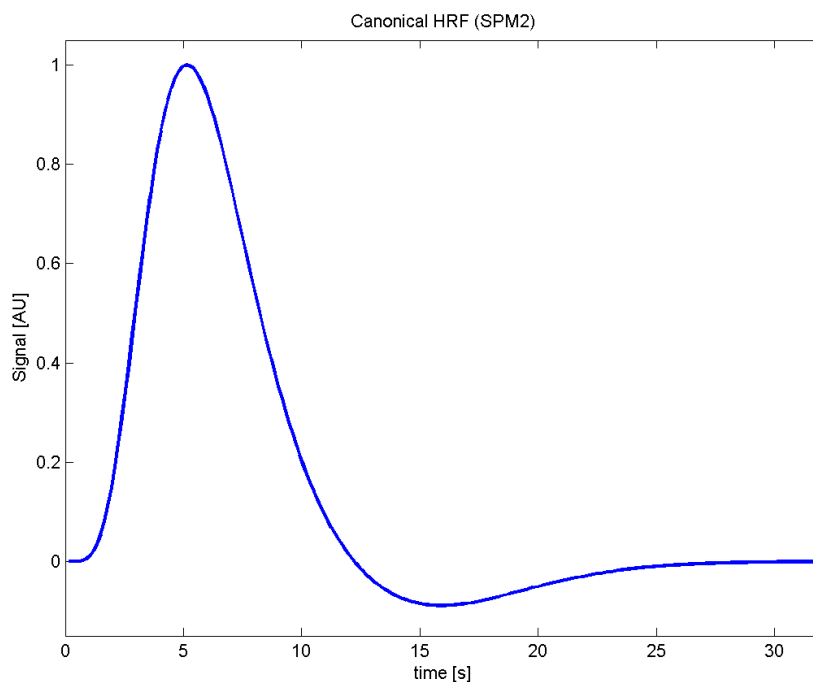


Figure 2.9: Canonical HRF used in SPM2 to model the BOLD response. Note that the post stimulus undershoot is modelled but not the initial dip.

³ SPM2 is a software package for functional neuroimaging by the Wellcome Department of Imaging Neuroscience at Queens Square University College London

⁴ Volterra kernels allow to perform non-linear convolution by considering history effects (past values) using an extended Taylor expansion.

3 Methods

This chapter describes the basics of the theory used for analysis of functional MR data. The steps and methods herein are largely based of the functionality that the software package BrainVoyager by Brain Innovation B.V. offers⁵. However, in cases where BV proved insufficient the descriptions are based on developed software or alternatively other software packages such as SPM2⁶ and FSL⁷. Developed software is written in Matlab (MathWorks, Natick, Massachusetts).

3.1 Hypothesis Driven Methods

Hypothesis driven methods refer to the use of methods that test whether a specified (expected) activation scheme fits the recorded data.

3.1.1 Linear Cross Correlation Analysis

A linear cross correlation analysis is basically the process of comparing the data to a defined reference. The correlation coefficient r_{xy} can be found as shown in equation (3.1), where x is the reference signal and y is the data. The sum over indices runs up to the no. of time points. A lag l has been introduced that shifts the reference time series by l samples. The denominator is essentially a scaling constant that normalizes the maximum possible correlation coefficient to 1 (y identical to x). The time series can either be assumed circular, in which case the index $i+l$ is interpreted $i+l$ modulus N (N being no. of time points), or the non-existing time series can be omitted ($x = 0$, $i + l > N$). The cross correlation is calculated at each voxel with a defined number of lags, then by noting the lag yielding the

⁵ For further information refer to the company webpage: www.brainvoyager.com

⁶ SPM2 is developed by collaborators from the Wellcome Department of Imaging Neuroscience at Queens Square University College London. Refer to [25] or the webpage: <http://www.fil.ion.ucl.ac.uk/spm/>

⁷ FSL is developed at the Oxford Centre for Functional Magnetic Resonance Imaging of the Brain (FMRIB). Refer to the website for further information: www.fmrib.ox.ac.uk/fsl/

maximum cross correlation along with the cross correlation itself it is possible to determine the phase and fit of the response [5].

$$r_{xy}(l) = \frac{\sum_i (x_{i+l} - \bar{x})(y_i - \bar{y})}{\sqrt{\sum_i (x_i - \bar{x})^2} \sqrt{\sum_i (y_i - \bar{y})^2}} \quad (3.1)$$

3.1.2 General Linear Model

$$y(t) = x_1(t)\beta_1 + \dots + x_N(t)\beta_N + \varepsilon(t) \quad (3.2)$$

Equation (3.2) shows a multiple linear regression of the signal $y(t)$ with N predictor variables, the term linear refers to the sum over each of the predictor variables $x_i(t)$. The coefficients for each predictor β_i are found by minimizing the residual sum of squares $\left(\sum_t \varepsilon^2(t)\right)$. Multiple regression analysis is performed for each voxel in a univariate fashion. A multiple regression analysis is basically a General Linear Model (GLM), however, the GLM allows multiple independent variables and linear transformations and combinations of dependent variables. Also multivariate test can be done in the GLM. The general assumption in the GLM is that the residual is independent and Gaussian distributed with zero mean.

The analysis formulated (more general) as a GLM using matrix notation is shown in equation (3.3).

$$\mathbf{Y} = \mathbf{X}\boldsymbol{\beta} + \boldsymbol{\varepsilon} \quad (3.3)$$

The GLM method for analyzing functional brain data was first adapted by Friston et al. in 1990 [28].

If \mathbf{X} has full rank the maximum likelihood estimate for $\boldsymbol{\beta}$ is given in equation (3.4), in the case of a singular design matrix constraints must be specified to obtain a pseudo inverse $(\mathbf{X}^T \mathbf{X})^-$ instead of $(\mathbf{X}^T \mathbf{X})^{-1}$.

$$\hat{\boldsymbol{\beta}} = (\mathbf{X}^T \mathbf{X})^{-1} \mathbf{X}^T \mathbf{Y} \quad (3.4)$$

It should be noted that the approach used in this study (and in the literature) is still essentially univariate in the estimation of parameters. The result is one beta value for each voxel that can be interpreted as a Statistical Parametric Map (SPM).

The columns of the design matrix \mathbf{X} specify the predictors and the rows correspond to the samples (time axis). The design matrix may contain both effects of interest and confounding predictors.

3.1.3 Correction for Serial Correlations

As indicated in section 3.3 on page 19, noise in fMRI data may be strongly temporally correlated. The presence of serial autocorrelations can be detected by the Durbin-Watson test⁸. An autoregressive (AR) process of order p can be modelled as shown in equation (3.5), where $x(t)$ is the signal, ϕ_i is the i 'th AR coefficient and $\varepsilon(t)$ is residual white noise.

$$x(t) = \phi_1 x(t-1) + \phi_2 x(t-2) + \dots \phi_p x(t-p) + \varepsilon(t) \quad (3.5)$$

In fMRI data positive temporal autocorrelation is usually present (see figure 3.1) meaning that a value in the time series (as compared to the baseline level) is likely to be followed by a similar value.

Temporal autocorrelation is a violation of the assumptions in the GLM as temporal independency of the residual is assumed.

One might argue that the use of a GLM is not even appropriate [2,102], however, it can be shown [31,100,101] that the parameter estimates remain essentially unbiased in the presence of serial autocorrelations. However, the variance will be underestimated meaning that the null hypothesis (see section 3.1.4) is rejected more easily (too many voxels are declared active). BrainVoyager first uses a standard least squares method to find the unbiased parameter estimates and then corrects for serial autocorrelations in the residual using a first order AR model (ϕ_1 is estimated for each voxel). The model is then refitted to determine the variance of the parameter estimates.

In the case of residual serial autocorrelation we have $\boldsymbol{\varepsilon} \sim N(0, \sigma^2 \mathbf{V})$. In this case a square non-singular matrix \mathbf{K} exist, so that $\boldsymbol{\varepsilon} = \mathbf{K}\boldsymbol{\varepsilon}_2$ and $\mathbf{V} = \mathbf{K}\mathbf{K}^T$ where $\boldsymbol{\varepsilon}_2 \sim N(0, \sigma^2 \mathbf{I})$ [99].

The general idea is now to estimate \mathbf{V} ⁹. The parameter variance is then given by $\sigma^2(\mathbf{c}^T \boldsymbol{\beta}) = \sigma^2 \mathbf{c}^T (\mathbf{X}^T \mathbf{X})^{-1} \mathbf{X}^T \mathbf{V} \mathbf{X} (\mathbf{X}^T \mathbf{X})^{-1} \mathbf{c}$ [29].

However, the variance does not follow a standard χ^2 distribution because of \mathbf{V} and the effective degrees of freedom must be altered accordingly [2,29-31,99,100,102],

⁸ $V = \sum_{i=2}^n (\varepsilon_i - \varepsilon_{i-1})^2 / \sum_{i=1}^n \varepsilon_i^2$, $V=2$ means no autocorrelation, $V<2$ indicates positive 1st order autocorrelation and $V>2$ indicates negative 1st order autocorrelation.

⁹ In SPM2 the estimate of \mathbf{V} is global (the same for all voxels). \mathbf{V} is modelled as $\mathbf{C}_Y = \mathbf{X}\boldsymbol{\beta}\boldsymbol{\beta}^T \mathbf{X}^T + \sum_i \lambda_i \mathbf{Q}_i$ Where \mathbf{C}_Y is the covariance matrix and \mathbf{Q}_i is the covariance matrix based on a AR model of order i . The coefficients λ_i is estimated using restricted maximum likelihood [29,100].

in relation to this it should be noted that BrainVoyager in contrast to SPM2¹⁰ does not correct the degrees of freedom.

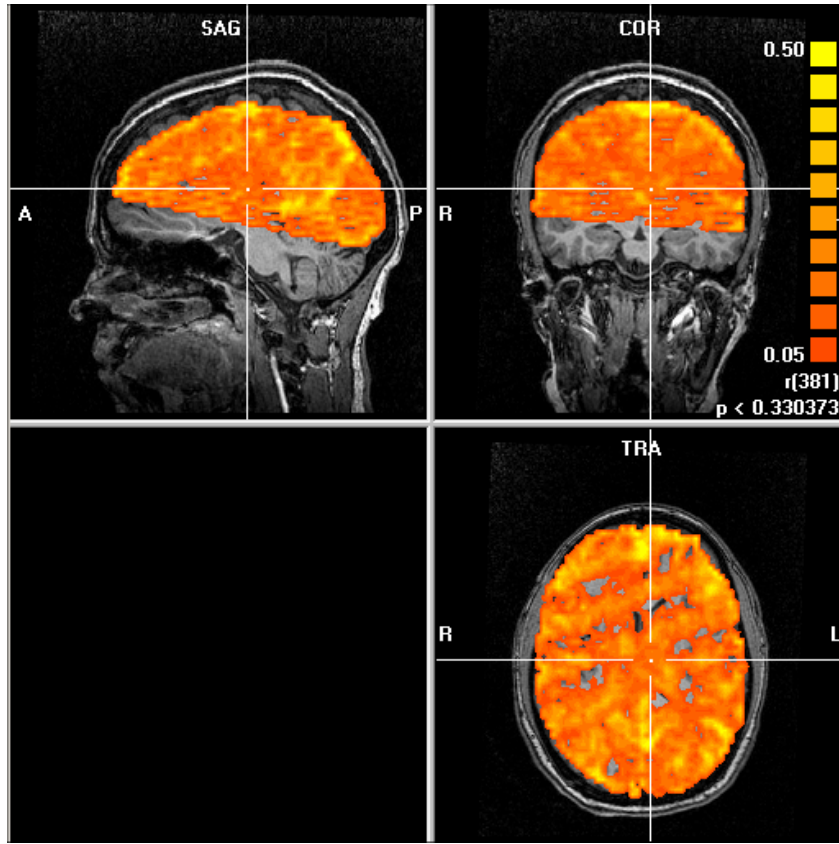


Figure 3.1: The spatial distribution of residual AR(1) coefficients, it is seen that positive serial auto-correlation is present in the vast majority of voxels.

¹⁰ The effective degrees of freedom (ν) is corrected according to the Satterwaite approximation: $\nu = \text{trace}(\mathbf{R}\mathbf{V})^2 / \text{trace}(\mathbf{R}\mathbf{V}\mathbf{R}\mathbf{V})$ where $\mathbf{R} = \mathbf{I} - \mathbf{X}(\mathbf{X}^T\mathbf{X})^{-1}\mathbf{X}$ [100]

3.1.4 Inferences in the GLM

The SPM containing the beta values is normally tested against the null hypothesis, that is, a hypothesis assuming no activity in any voxel. The idea is to reject the hypothesis for the activated voxels using an F- or t-test. By incorporating the concept of contrasts, different combinations of the predictors can be tested¹¹ and compared to the value in the corresponding distribution with the appropriate degrees of freedom.

Correcting for Multiple Comparisons

For each voxel a hypothesis test is performed. Because of the many voxels across the brain it is necessary to correct the p-values for multiple comparisons. This can be achieved by using Bonferroni correction (all observations assumed independent), however, this does not take the spatial correlation into account. Nearby voxels are clearly correlated in the fMRI data, therefore the corrected probabilities based on Bonferroni correction would be way too conservative. The correction implemented in BrainVoyager is the FDR (false discovery rate) where the basic idea is to perform Bonferroni correction on the number of voxels declared active.

First the P -values (uncorrected, V values in total) are ordered according to equation (3.6).

$$P_{(1)} \leq P_{(2)} \leq \dots \leq P_{(V)} \quad (3.6)$$

Now voxels for which equation (3.7) holds are declared active, the value q is the selected FDR.

$$P_{(i)} \leq \frac{i}{V} \frac{q}{C(V)} \quad (3.7)$$

The choice of the predetermined constant $C(V)$ is based on the joint probability distribution of P over voxels. For independence across voxels and non negative Gaussian noise correlation in the data $C(V) = 1$, for any joint probability distribu-

¹¹ t-test statistics tests the hypothesis: $H_0 : \mathbf{c}^T \boldsymbol{\beta} = 0$ yielding the ordinary students t statis-

tics: $t = \frac{\mathbf{c}^T \hat{\boldsymbol{\beta}}}{\hat{\sigma}_i(\mathbf{c}^T \hat{\boldsymbol{\beta}})} = \frac{\mathbf{c}^T \hat{\boldsymbol{\beta}}}{\sqrt{\sigma_i^2 \mathbf{c}^T (\mathbf{X}^T \mathbf{X})^{-1} \mathbf{X}^T \mathbf{V} \mathbf{X} (\mathbf{X}^T \mathbf{X})^{-1} \mathbf{c}}}$ where \mathbf{c} is contrast and $\hat{\sigma}_i(\mathbf{c}^T \hat{\boldsymbol{\beta}})$

denotes the variance estimate (for voxel i).

F-test statistics similarly tests the hypothesis: $H_0 : \mathbf{c}^T \boldsymbol{\beta} = 0$ with the ordinary F statistics:

$F = \frac{\text{additional variance described by effects of interest}}{\hat{\sigma}_{\epsilon,i}}$ where $\hat{\sigma}_{\epsilon,i}$ denotes the estimated

residual variance taking serial autocorrelation into account.

tion across voxels the linear approximation $C(V) = \ln(V) + \gamma$ is used where gamma is the Euler constant approximately equal to 0.5772 [34].

SPM2 has yet another option for correction of multiple comparisons based on random field theory. This correction type assumes the SPM to follow a Gaussian random field, however this requires data to be smooth across approximately 10 voxels (FWHM¹²) to be accurate [57].

3.2 Data Driven Methods

Methods that do not assume any activation scheme for testing for activity are known as data driven methods.

3.2.1 Independent Component Analysis

Independent Component Analysis (ICA) is a mathematical method of doing blind source separation by assuming statistical independence for the sources, this was suggested and implemented for fMRI data in 1998 by McKeown et al. [53-55]. As opposed to Principal Component Analysis (PCA), ICA finds components in the data that are not necessarily orthogonal but rather statistically independent.

In case of high dimensionality in the input data, Singular Value Decomposition (SVD) is normally used to reduce the dimensionality of the input data before the ICA is done. SVD is basically the process of identifying the directions of maximum variance¹³.

Assuming linear mixing, the problem can be formulated as shown in equation (3.8), where X_{jt} is the signal at voxel j at time t . The coefficients A_{jk} (maps) describe the weight of each of the time series S_{kt} . K is the number of components.

E_{jt} is the residual spatial and temporal white noise.

$$X_{jt} = \sum_{k=1}^K A_{jk} S_{kt} + E_{jt} \quad (3.8)$$

In case of spatial ICA, statistical independence is assumed on the columns of the matrix \mathbf{A} (consisting of the component A_{jk}). Similarly, temporal ICA is performed by assuming statistical independence upon the rows of the matrix \mathbf{S} . Differences between spatial and temporal ICA have been addressed by various authors see for

¹² Full Width at Half Maximum

¹³ SVD here performs a Principal Component Analysis based on the covariance matrix. This is the process of finding eigenvectors of the covariance matrix and sorting them based on the eigenvalues (variances).

example [11]. The ICA algorithm finds statistically independent components in the signal. In this study the FastICA algorithm[43] will be used to do spatial ICA. FastICA is based on maximization of statistical higher order moments (4th order moment, kurtosis). For this reason the input data have to be non-Gaussian, this is however not a limitation in practice. To visualize the results of ICA both the maps (A_{jk}) and the time series (S_{kt}) are used. [22,52-55]

3.3 Noise

Besides the actual BOLD signal, the data also contain components from sources such as movement, edge artifacts, cardiac- and respiratory effects. Also signal components related to instability and drift in the scanner hardware are common in fMRI data. As all these effects are undesirable in the context of analysing and locating brain activity, we will label all these effects noise in the following. [36]

Noise is consequently a very prominent factor in fMRI data, and what worsens the situation even further is that the noise may be both temporally and spatially distributed. Figure 3.2 shows a typical example of noise in recorded fMRI data. The power spectrum in figure 3.3 clearly indicates that the noise does not resemble white noise. This poses a problem in subsequent statistical data analysis as one usually assumes that the residual is temporally independent. It should be noted that there is a clear increase in the noise at low frequencies, probably related to drift in the scanner hardware [76].

The cardiac cycle induces movement (pulsation) in the brain that is most severe near large blood vessels. Because this signal is heavily undersampled, the slightly varying frequency will be aliased¹⁴, thus having the appearance of noise in the time series. The respiratory cycle is also undersampled during normal circumstances where the effect is mostly gross movement resulting in most prominent effects at the edges.

¹⁴ Aliasing is the unpleasant phenomenon of undersampled frequencies occurring at frequencies from zero to the Nyquist frequency. Let $f = n f_s/2 + \varepsilon$ be the signal frequency where n is the largest integer to make $0 \leq \varepsilon < f_s/2$ and f_s be the sampling frequency then the aliased frequency will be given by:

$$f_a = \begin{cases} \varepsilon & \text{for } n \text{ even} \\ \frac{f_s}{2} - \varepsilon & \text{for } n \text{ odd} \end{cases}$$

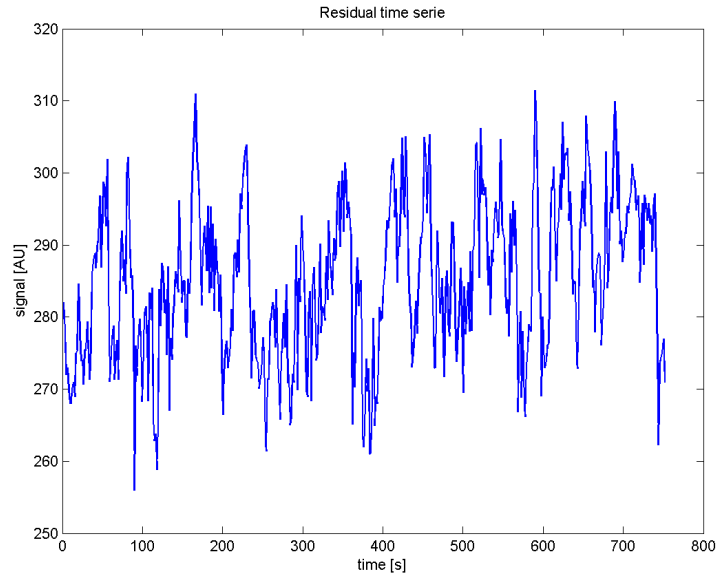


Figure 3.2: Noise in fMRI time series. The figure shows the residual (effects of interest removed) time series of a grey matter voxel. The data is sampled at a frequency of $(1/1.55)$ Hz.

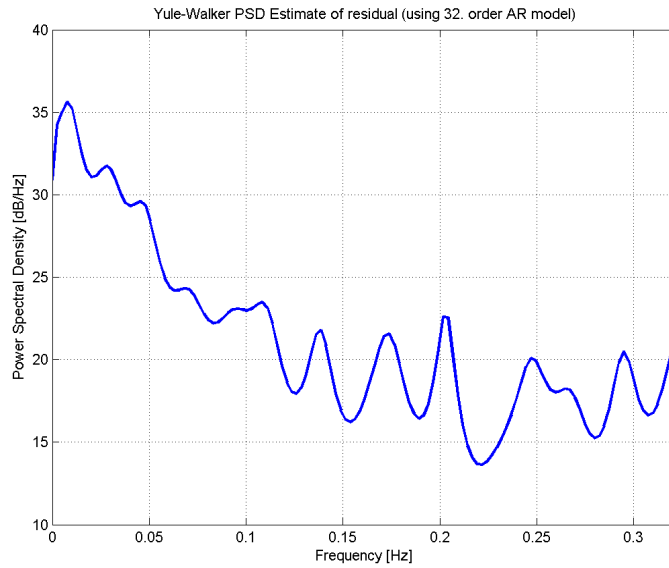


Figure 3.3: Estimated frequency power spectrum for the time series shown in figure 3.2 (corrected for the mean value). The spectrum is estimated using the Yule-Walker AR method; this method uses an estimation of the autocorrelation coefficients to generate the power spectrum [51]. This method is generally more robust than direct estimation for data with low SNR. Here autocorrelation coefficients up to 32nd order are estimated from a Fast Fourier Transform with the length 256. Note that noise power increases at lower frequencies, also note that the power is given in dB (semi-logarithmic plot). This plot is in general agreement with what is found in the literature (see for example [76,89]).

3.4 Pre-processing Functional Data

The following provides a short introduction to the most common pre-processing steps and describes some advantages and disadvantages related to each step.

The term pre-processing refers to the process of altering data before the statistical analysis to remove at least part of the confounders described in section 3.3. The choice of parameters for each pre-processing step is ambiguous and it may even be appropriate to skip some pre-processing steps.

3.4.1 Motion Correction

Even minor movements during an fMRI experiment severely degrade the quality of the signal. The main reason is that some voxels will be moved to another part of the brain possibly with a very different signal intensity (for example moving a white matter voxel into grey matter or vice versa). For the same reason this effect is normally most prominent near the edges of the head and near the ventricles¹⁵, an example of the spatial distribution of these effects is seen in figure 3.4.

The signal contamination due to movement may be reduced greatly by the use of a 6 parameter rigid body transformation (displacement and rotation) [33]. The determination of the optimal parameters is possible by minimizing the sum of squares intensity difference from a reference volume. BrainVoyager uses the Levenberg-Marquardt algorithm¹⁶ for the least squares fit or switches to steepest descent if the algorithm fails. To calculate the intensity of subvoxel coordinates in a transformed image BrainVoyager offers the possibility to use either trilinear¹⁷ or sinc¹⁸ interpolation. Sinc interpolation is expected to be the preferred choice, but as the difference between the two is negligible in practice, the much faster trilinear interpolation is normally used.

Even after motion correction there might still be residual motion left in the data due to field inhomogeneities. This issue has been addressed by Friston et al. [33] where a method for estimating the effects of movement and correction thereof is described. The idea is to correct for movement by introducing predictors related to movement in the GLM. The methods suggest the use of the following parameters:

¹⁵ Compartments in the brain containing CSF, these will appear white (large signal) in BOLD weighted images.

¹⁶ The Levenberg-Marquardt algorithm allows the iteration to reach the minimum faster than standard steepest descent by assuming the least square function can be quadratically approximated near the minimum.

¹⁷ Trilinear interpolation is the process of linearly interpolating points within a 3D box given values at the vertices of the box.

¹⁸ 3 dimensional sinc interpolation can be performed in the frequency domain by null filling higher frequency components.

1. The 6 motion parameters (translation and rotation) (linear effects).
2. The same 6 parameters squared, this account for effect that are the same for movement in both directions (e.g. a white matter voxel between two grey matter voxels).
3. The 6 motion parameters from the previous volume to account for spin-history effects.
4. The 6 motion parameters from the previous volume squared.

An F-test over the effects of residual motion can be seen in figure 3.4.

The Siemens Trio scanner is capable of automatically motion correcting the recorded images (both the corrected and the uncorrected version is available). Furthermore, a real time motion correction algorithm also known as Prospective Acquisition CorrEction (PACE) [79] is available estimating transformation parameters while scanning and adjusting the gradients accordingly.

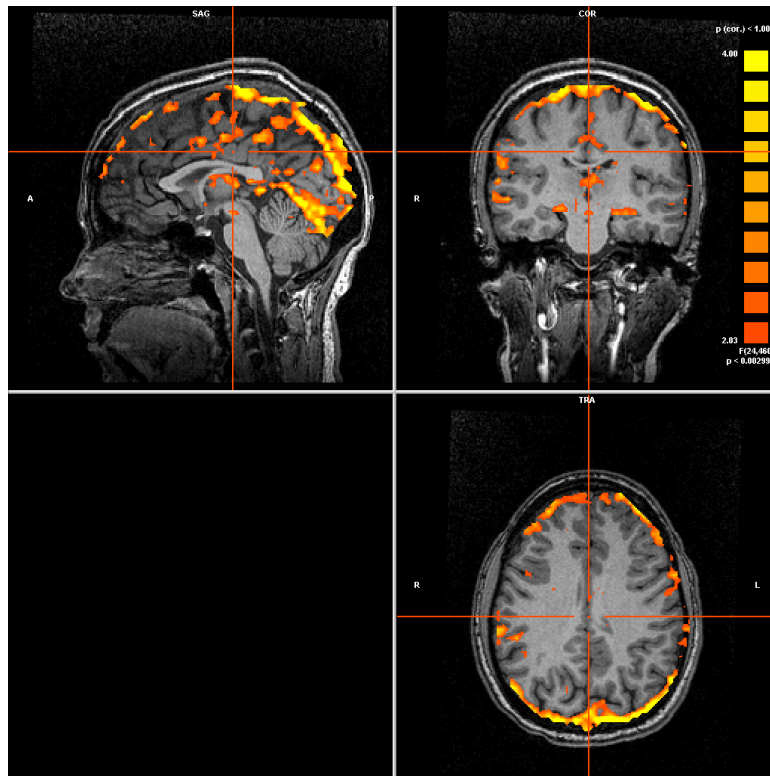


Figure 3.4: Spatial distribution of motion related artifacts. The image is generated by using an expansion of the parameters from the motion correction process as predictors in a GLM as suggested by [33] (24 predictors used). Voxels with p -values higher than 0.05 (FDR corrected) are considered significant (colorscale for the F-values are displayed to the upper right). The SPM has been interpolated (trilinear) to $1 \times 1 \times 1$ mm for visualization. It should be noted that the data has already been corrected for movement by a 6 parameter rigid body transformation; this strongly indicates that residual motion is still present in the data after motion correction.

3.4.2 High Pass Filtering

For reasons described in section 3.3, it is desirable to remove low frequencies in the data before the analysis [76], which can be done by applying a high pass filter.

In SPM2 this process is performed by fitting a GLM consisting of discrete cosine functions to the data and subtracting the reconstructed signal from the original signal. The first predictor completes half a cycle in the time series, the following are separated by half a cycle until the cut-off frequency is reached.

The cut off frequency for the high pass filter should optimally depend on the specific scanner hardware (the optimal parameters could be found by analysing time series consisting of only noise), however the standard approach is to use a standard cut off frequency. The default cut-off frequency in SPM2 is 1/128 Hz.

BrainVoyager first uses a linear trend removal with a subsequent standard high pass filter in the Fourier domain.

Due to high pass filtering it is important that the effects of interest occur at frequencies higher than the cut off frequency.

3.4.3 Slice Time Correction

The slices in an fMRI experiment are recorded one slice at a time resulting in different acquisition time for each slice. A complication of this time delay is that the slices are usually recorded interleaved to reduce crosstalk between slices. However, to simplify the analysis it is usually assumed that all slices are recorded simultaneously. This assumption might cause problems especially in the case of fast shifting paradigms (event related). To overcome this problem the time series for each voxel is resampled according to the acquisition time of the voxels in a reference slice. The interpolation method is normally standard sinc interpolation¹⁹ meaning that exact interpolation is achieved if the signal is band-limited and only contains frequency components lower than the Nyquist frequency²⁰. This condition is obviously violated in fMRI data as both cardiac activity and respiration usually occur at frequencies higher than or near the TR frequency.

Despite the problems related to slice time correction this process normally seems to improve the timing in the data and is therefore a common pre-processing step.

¹⁹ 1 dimensional sinc interpolation is done in the time domain by convolving the sampled signal with the sinc function. $\text{sinc}(x) = \begin{cases} \sin(x\pi)/(x\pi) & , x \neq 0 \\ 1 & , x = 0 \end{cases}$

²⁰ In order to fully reconstruct a band-limited signal (maximum frequency component f_{\max}) it must be sampled at the Nyquist frequency or higher ($f_{\text{Nyquist}} = 2f_{\max}$). In the absence of noise no information is gained by sampling faster than the Nyquist frequency (oversampling).

3.4.4 Smoothing

The strong traditions for spatial smoothing of data in multi subject experiments exist for several reasons. Spatial smoothing reduces non-spatially distributed noise by averaging neighbouring voxels. Also the smoothing process may help to reduce differences between subjects. The drawback of smoothing is that the spatial resolution of the images is compromised. In single subject experiments spatial smoothing is normally omitted to keep the maximum resolution in the images. Smoothing is usually done by convolving with a Gaussian kernel/function.

Temporal smoothing can be considered in some cases, as it also reduces the noise. Because the BOLD response is already quite temporally extended the penalty in terms of timing may not be great. Another problem is that temporal smoothing introduces severe autocorrelation (see section 3.1.3). It should be noted that the introduced autocorrelation is known, meaning that it is possible to perform correction in the statistical model. In the earlier version of SPM2 (SPM99) the serial autocorrelations were dealt with by using a low pass filter (temporal smoothing) and then correcting the known (introduced) autocorrelation.

3.5 Processing Anatomical Data

Functional volumes can be acquired very fast (typically within 2-3 seconds) however they are not suitable for defining anatomical features. To account for this an additional high resolution (1x1x1 mm) anatomical volume is usually acquired. By overlaying the activation from the statistical analysis of the functional scan, anatomical localization of the activity is possible. Also the anatomical image provides a possibility of distinguishing white and grey matter.

Activity is (at least to a large extent) restricted to grey matter, largely located in a layer near the edges of the brain. This cortical grey matter represents a highly folded structure as seen in figure 3.5. Because activity is expected to be spatially extended along this folded structure it is preferable to display the activation on an unfolded representation of this cortical layer. This process of constructing an unfolded shape is known as cortical flattening.

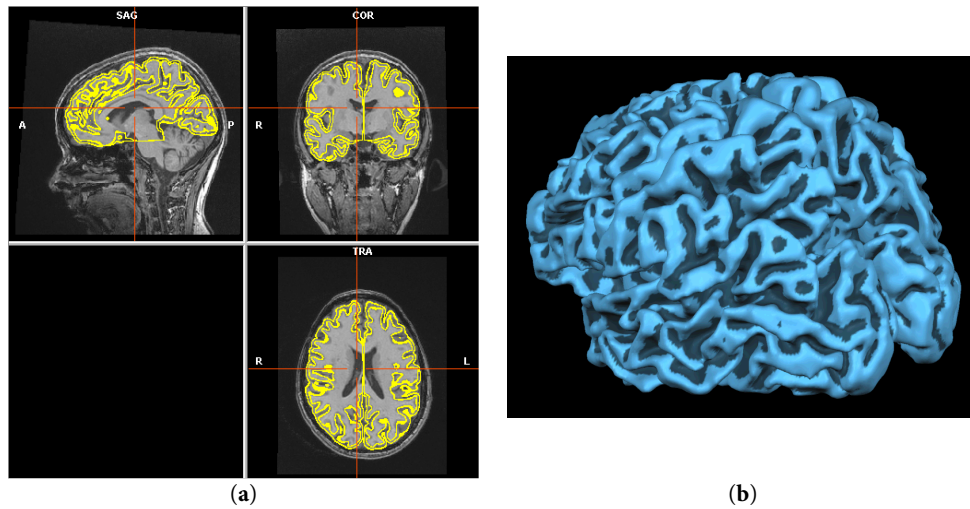


Figure 3.5: Cortical grey matter. Figure (a) shows the layer of grey matter as two yellow lines superimposed onto the image, the inner surface of grey matter is shown as 3D projection in figure (b). The surface reconstruction has been performed using the method described in the following sections.

3.5.1 Normalization

Normalization is the process where the anatomical image is transformed into a standard space. The main reason for doing so is to make a rough pre-segmentation possible using a simple standard brain mask. This normalization also provides the possibility of identifying coordinates with respect to a standard anatomical atlas.

In BrainVoyager the standard template is the widely used Talairach atlas [78]. The normalization is done by defining 8 anatomical landmarks used to construct a 4x4 transformation matrix²¹. It should be noted that this transformation is relatively crude compared to the method used in SPM2 [26].

3.5.2 Inhomogeneity Correction

Because of spatial variations in the sensitivity of the receiving head coil, tissue has different intensities according to the position within the head coil. This effect is especially pronounced in surface coil arrays. In order to correct for this difference in intensity, an inhomogeneity correction is performed before the segmentation into grey and white matter. In BrainVoyager the 3D bias field is estimated by fitting Legendre polynomials to an initial white matter segmentation. The initial segmentation is performed by a region growing process on the uncorrected data [92]. An example of an estimation of the bias field can be seen in figure 3.6. With-

²¹ The translation process consists of translation, scaling and rotation but not shear.

out performing inhomogeneity correction, it proved impossible to perform reasonable white matter segmentation.

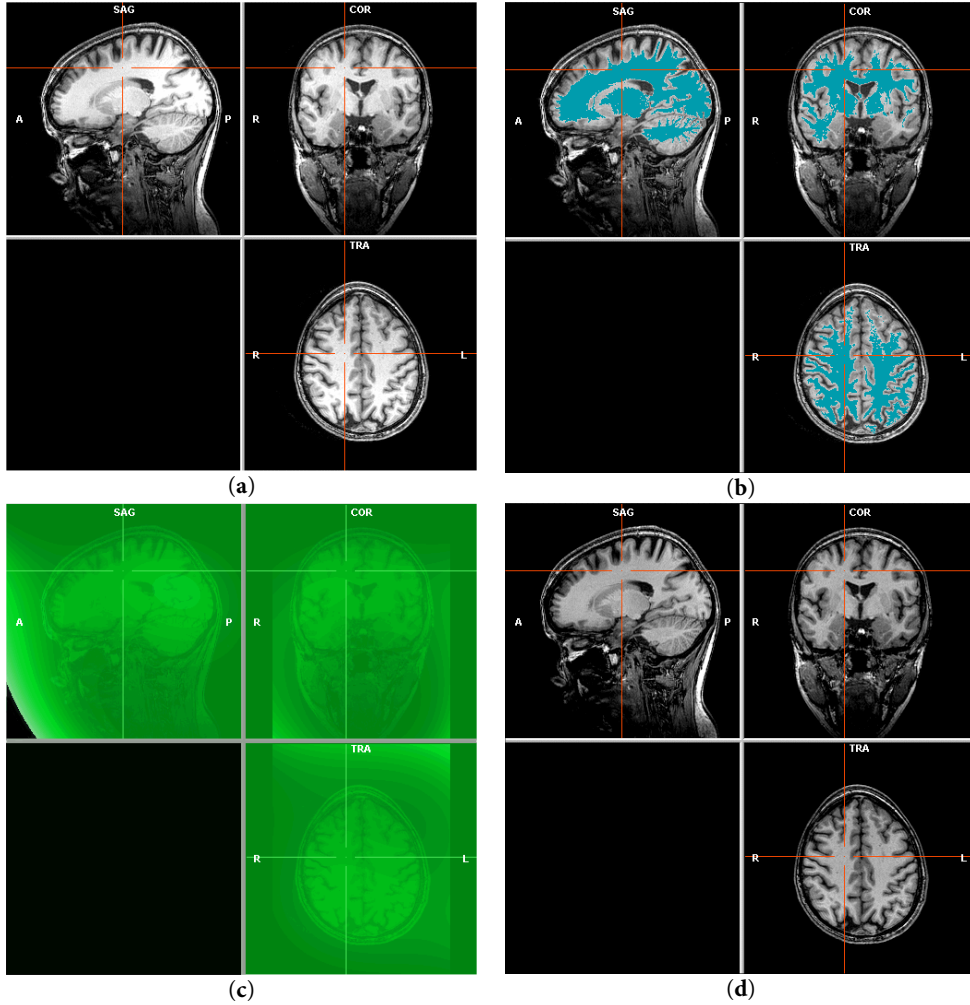


Figure 3.6: Inhomogeneity correction. Figure (a) shows the original image (before inhomogeneity correction). Figure (b) shows an initial crude white matter segmentation used to estimate the bias field illustrated in (c). In (c) the bias field is shown in a green colour scale with the original image alpha blended onto it. Finally figure (d) shows the image after inhomogeneity correction. This anatomical scan has been acquired by the standard MPAGE sequence described in section 4.1.3 using a surface coil array with 8 elements. The original signal intensity is high in the far occipital part of the brain. It should be noted that this illustration only partly mimics the bias field's extension in all 3 dimensions.

3.5.3 Segmentation

Because segmentation into grey and white matter provide the basis for creating the unfolded representation, it is important that this process is as accurate as possible.

A full description of the process is beyond the scope of this text, but the following will briefly introduce the steps involved in performing segmentation in BrainVoyager.

1. Data are filtered using an edge preserving sigma filter [46,49] to ease the later segmentation process by reducing the number of topological defects initially present [13].
2. Ventricles are located and filled; this process is done to avoid topological defects in the segmentation (holes) in these areas.
3. A Talairach brain mask is applied to remove skull and other non brain regions. This is done to avoid the region growing process to advance into these regions.
4. The white matter is found by region with a given threshold growing with a seed point known to be located inside the white matter structure.
5. Dilation and smoothing of white matter is then performed to ensure that the curvature is finite at all points.
6. Disconnection of the two hemispheres.
7. This step is performed to correct for topological errors (handles) from the segmentation in step 4. The region growing process is redone now using self-touch sensitive algorithm meaning that the outer boundaries of the region are not allowed to merge with itself and form rings. This produces a white matter segmentation free from topological defects (handles), however the result will be biased because the algorithm is only able to exclude voxels. To account for this the same process is performed for the inverse object yielding the opposite result (only inclusion of voxels). For each of the corrections the damage compared to the original segmentation²² is estimated and the choice yielding the least damage is chosen [46]. The resulting region is sure to be free of topological errors.

An example of the segmentation result is shown in figure 3.5a.

²² The original segmentation is a simple threshold between grey and white matter, the damage of changing a voxel is dependent on the deviation from this threshold.

3.5.4 Inflation

Once the cortex has been segmented, a mesh is folded onto the boundary between white and grey matter. Because of the smoothing and dilating process described in 3.5.3, this mesh should conform to a region within grey matter. In principle the activations could be overlaid on this mesh. However, because of the highly folded structure an overview of the activation is hard to achieve. To account for this, the mesh is inflated while trying to keep the original metric properties. The process involves the use of an energy function with a spring term that smoothes the surface and a metric-preservation term that incorporates both distances²³ and area. The minimum of the energy function is estimated using an iteration scheme gradually yielding the desired shape.

This energy function and the inflation process in general is described in detail in [24]. An example of an inflated mesh can be seen in figure 3.7.

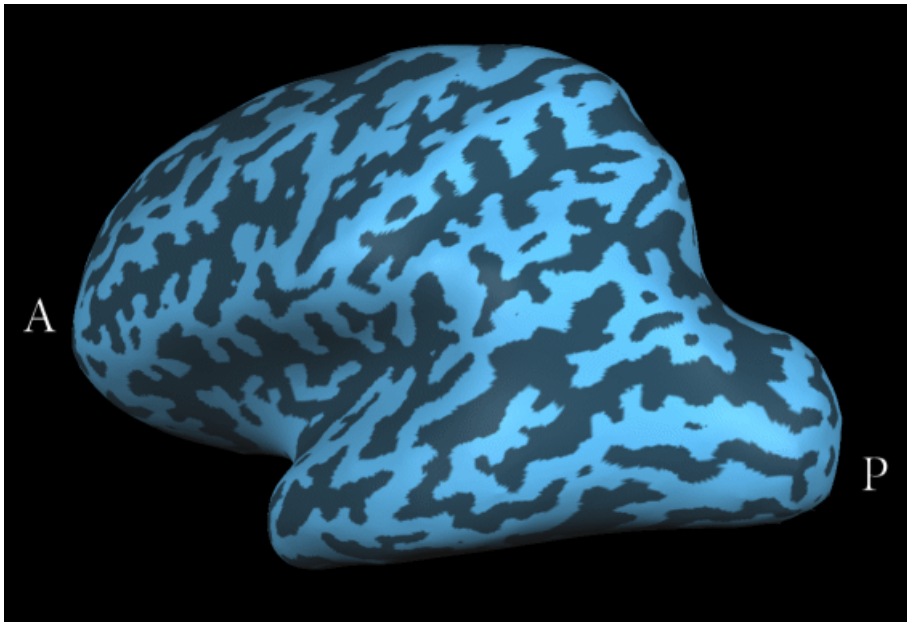


Figure 3.7: The figure shows an example of an inflated left hemisphere mesh using the BrainVoyager software, the darker colour represent regions which had negative curvature in the original folded surface. The smoothing force coefficient used was 0.8. The original surface curvature has been overlaid.

²³ As distance computations on surfaces containing many vertices faces is very computationally intensive the Dijkstra algorithm is used, this algorithm yields an overestimate of the distances. This bias estimate is then corrected by a scaling factor to obtain an unbiased estimate (white noise with zero mean deviation from the true distance)[24].

3.5.5 Unfolding

The inflated mesh shown in figure 3.7 is useful to provide an overview of the brain surface, however to achieve an unfolded representation another step must be completed. The cuts used to unfold the mesh are defined as shown in figure 3.8, also showing the directions in which to unfold the mesh. BrainVoyager uses an automatic scheme for selection of cuts and unfolding vectors. To improve the localization of the cut along the CS a manual definition has been applied in this study. Finally, the surface is projected onto a plane (two sides), unfolding is now the process of warping the regions from the side on which the cuts were made onto the other side.

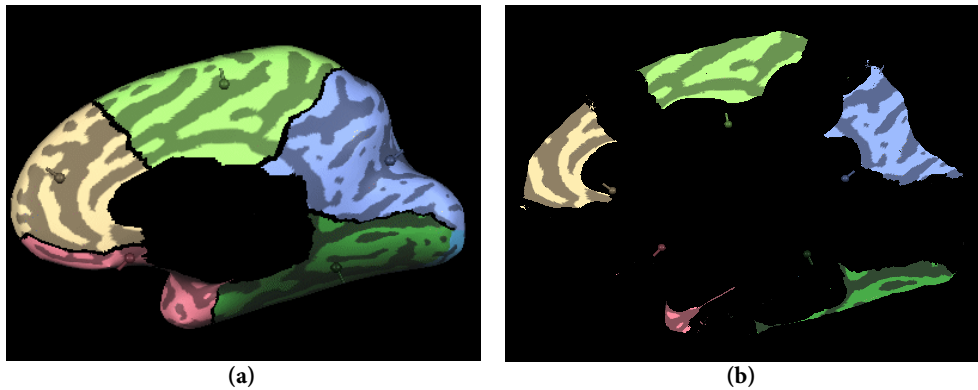


Figure 3.8: Figure (a) shows a medial view of the cuts and unfolding vectors (right hemisphere), the cut along the SC has been done manually. The area removed in the middle is not of importance as it represents WM and furthermore is the place where the cut between the two hemispheres has been done. The different regions has been coloured to allow identification when the mesh has been unfolded.

Figure (b) shows the partially unfolded mesh also viewed from the medial side.

3.5.6 Distortion Correction

The unfolded surface is now a flat representation of the cortical surface, however, the unfolding procedure has introduced distortions in the distances on the surface as compared to the original mesh (see figure 3.9). In order to reduce these distortions the vertices are moved iteratively to minimize a length distortion energy function as described in 3.5.4 [13,24]. The resulting mesh is a flat representation of the cortical grey matter where activation can be overlaid by using the original positions from the folded mesh for each vertex.

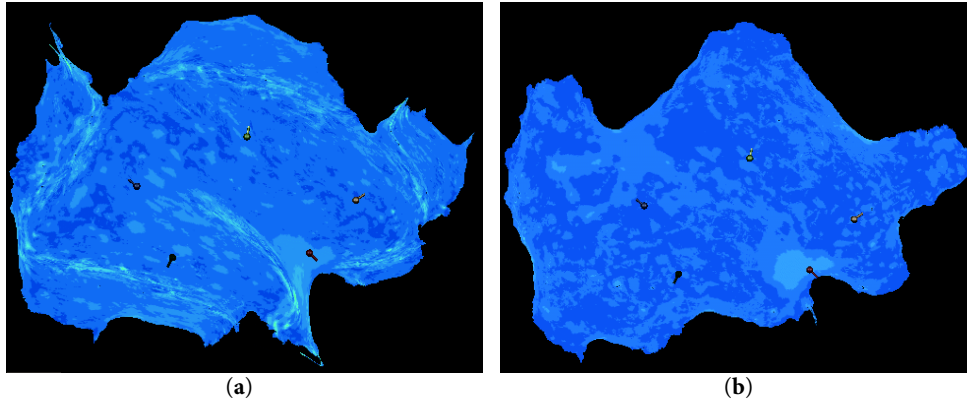


Figure 3.9: Figure (a) shows the result of unfolding of the right hemisphere, distortions are shown in a blue to green colour map note that distortions are most prominent in the region where the unfolding are done.

Figure (b) shows the same surface after distortion correction in the same colour map note that the distortions are reduced considerably.

3.5.7 Physiological Noise

Because physiological noise is one of the large confounders in fMRI, it is desirable to perform some kind of correction for it.

GLM method

The GLM method to correct for physiological noise used in this study is based on a time series of the physiological noise obtained during scanning. If the exact shape of the physiological noise effect was known it would simply be a matter of including a predictor in the GLM consisting of the measured physiological time series convolved with the known response function. However, first of all, this response function is not known (it might vary over subjects) and secondly the shape of the response might vary spatially over the brain. The method used is therefore a predictor (or rather a set of predictors) consisting of the time from last peak detected in the physiological time series for each measurement. This is illustrated in figure 3.10. This predictor is constructed for each slice obtaining a linear (saw tooth) shape. By including a predictor for each slice it is possible to model the expected actual response for each voxel [12]. This process is done for both respiration and cardiac data. The resulting predictors are shown in figure 3.11 [50].

It should be noted that by using this method a degree of freedom for the residual is lost for each slice (for each noise type)²⁴, this however does not constitute a large

²⁴ As the predictors are generally not orthogonal, the number of degrees of freedom lost are usually a little less.

problem as the total number of degrees of freedom is quite large in this study (around 300-400).

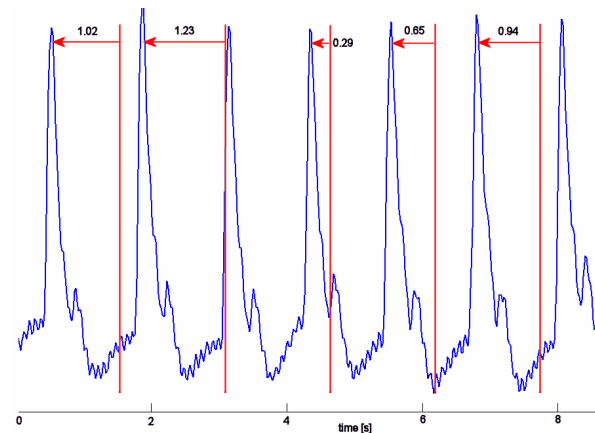


Figure 3.10: The figure shows the principle used to construct the predictors for accounting for physiological noise in the GLM. The time series plotted in blue is a typical (however rather low rate) cardiac²⁵ time series. The red lines denote each volume measurement, the values above are the values used in the predictor. This predictor is constructed for each slice obtaining a linear shape for each slice. By combining these it is possible to obtain other response shapes.

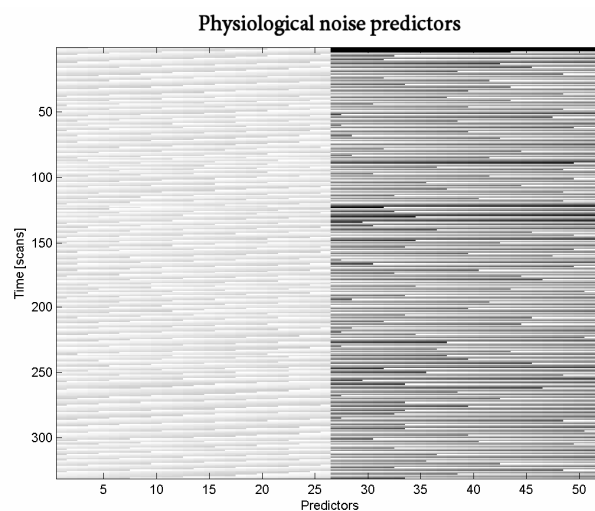


Figure 3.11: Predictors to account for physiological noise. The first 26 columns account for cardiac noise and the last 26 account for respiratory noise. The TR used was 1.55 s, the average no. of cardiac peaks per minute was 46 and the average no. of respiratory peaks per minute was 15.

²⁵ The cardiac cycle was measured as the blood oxygen content by measuring the light absorbed by the blood in the subjects' finger (in the infrared spectrum). This is a reliable method to measure cardiac data while scanning. The respiration cycle was obtained by using a pneumatic belt. Both are sampled at 50 Hz.

4 Experiments

This chapter provides a description of the most important experiments conducted in this study and presents the obtained results. The sections refer to the individual experiments.

4.1 Retinotopic Mapping

Retinotopic mapping refers to the process of delimitating the borders of the early visual areas. This has been done by a vast number of authors [3,18,20,38,68-71,73-75,81,87,91,98], however, due to the demanding post-processing and data analysis the procedure is still not commonly implemented. The first retinotopic mapping experiments were performed by [21] and [69] separately. The visual field sign (VFS) map method was suggested by Sereno in [69] and is now the standard way of delimitating the borders of the visual areas. The VFS is based on the Jacobian (J) of a mapping from the visual field to the visual cortex (also known as the visual field ratio). The Jacobian can be interpreted as the ratio between local areas (including sign/direction) in each of the coordinates. That is, the sign of the Jacobian tells whether the representation in the cortex is a mirror representation of the visual field. Having a mapping between points (u, v) on the flattened 2D representation of the cortex and the visual field coordinates $(\varphi_r, \varphi_\alpha)$ the Jacobian is defined as shown in equation (4.1). $\nabla_u \varphi_r$ denotes the radial phase gradient with respect to coordinate u in the cortex and so forth.

$$J = \frac{\partial(\varphi_r, \varphi_\alpha)}{\partial(u, v)} = \nabla_u \varphi_r \cdot \nabla_v \varphi_\alpha - \nabla_v \varphi_r \cdot \nabla_u \varphi_\alpha \quad (4.1)$$

The first problem is to obtain a mapping between coordinates in the visual field and in the visual cortex. This will be done using the experiment described in the following sections. [17,20,21,68-70,74,75,82,83,91,95,98]

4.1.1 Experimental Setup

The stimulus was displayed by means of a projector (Canon LV-7545) placed outside the Faraday cage. A zoom lens projected the image through a waveguide to a back-projection screen behind the subject's head. A mirror placed above the subjects eyes allowed them to look at the screen (38 cm x 29 cm) from a distance of 88 cm (l). At this distance the viewing angle was $\pm 9.2^\circ$ (E_{\max}) in the vertical direction and $\pm 12.2^\circ$ horizontal²⁶. The display resolution was 1024 (horizontal) by 768 (vertical) with 72 Hz refresh rate. The cardiac cycle was recorded using an infrared sensor placed on the subject's left hand index- or little finger at a sampling rate of 50 Hz. Similarly the respiratory cycle was monitored using a pneumatic belt also with a sampling frequency of 50 Hz. The stimulus was displayed using the IFIS system (Psychology Software Tools, Pittsburgh, USA).

Subjects were informed to report by pressing their right hand index finger when the fixation point changed colour from red to green. This change occurred at random time points with mean of 4.5s²⁷ between events.

²⁶ Eccentricities (E) are translated into distances on the screen (r) using the following relation: $r = l \tan E$

²⁷ The time between events was drawn from a uniform distribution in the range from 3 to 6s that is mean 4.5s and 0.87s standard deviation.

4.1.2 Visual Stimuli

To improve the perspectives for clinical use, the visual stimuli were designed using the software package E-prime (Psychology Software Tools, Pittsburgh, USA) already used at the scanner. The implementation is done completely in a script like language (inline scripting). A full description of the implementation is beyond the scope of this text but commented source code is provided on the web page.

Two types of visual stimuli were used: an eccentricity and a polar mapping. Both showed part of a circular flickering checkerboard reversing at 8 Hz²⁸, which through testing²⁹ and according to the literature [23,47] proved to produce good results.

The checkerboard was scaled according to cortical magnification. By separating the variables in equation (2.1) and integrating, one obtains the result given in equation (4.2).

$$\begin{aligned}\Delta x &= A \ln \frac{E_{end} + E_2}{E_{start} + E_2} \\ E_{end} &= e^{\frac{\Delta x}{A}} E_{start} + E_2 \left(e^{\frac{\Delta x}{A}} - 1 \right)\end{aligned}\tag{4.2}$$

E_{start} and E_{end} represent two eccentricities separated by the cortical distance Δx . The eccentricities were translated into positions on the screen as described in section 4.1.1

The constants used were $A=20$ mm and $E_2=0.5^\circ$ in agreement with the meta analysis from 2001 by Slotnick et al. [72]. Each check was scaled radially to cover 3 mm in the cortex, the checks covered a polar angle of 12° yielding a total of 30 slices (see figure 4.1a).

All parameters (including colours, constants and the timing parameters) can be changed easily (in a table) – no programming knowledge required.

Under the assumption that a given region in the cortex is only activated at one angle/radius combination it is possible to show the stimuli without any explicit baseline condition. This further yields the advantage that only retinotopic areas are mapped (activated), because the same activation disregarding position is present at all times during the paradigm.

²⁸ 8 Hz refers to the frequency of shifts (that is, for a full cycle the rate would be 4 Hz).

²⁹ An experiment was done to determine the optimal reversal rate the results, however, were somewhat inconclusive. There was not a sharp frequency peak but more of a range of frequencies between 6 and 40 Hz that showed to produce equally good results.

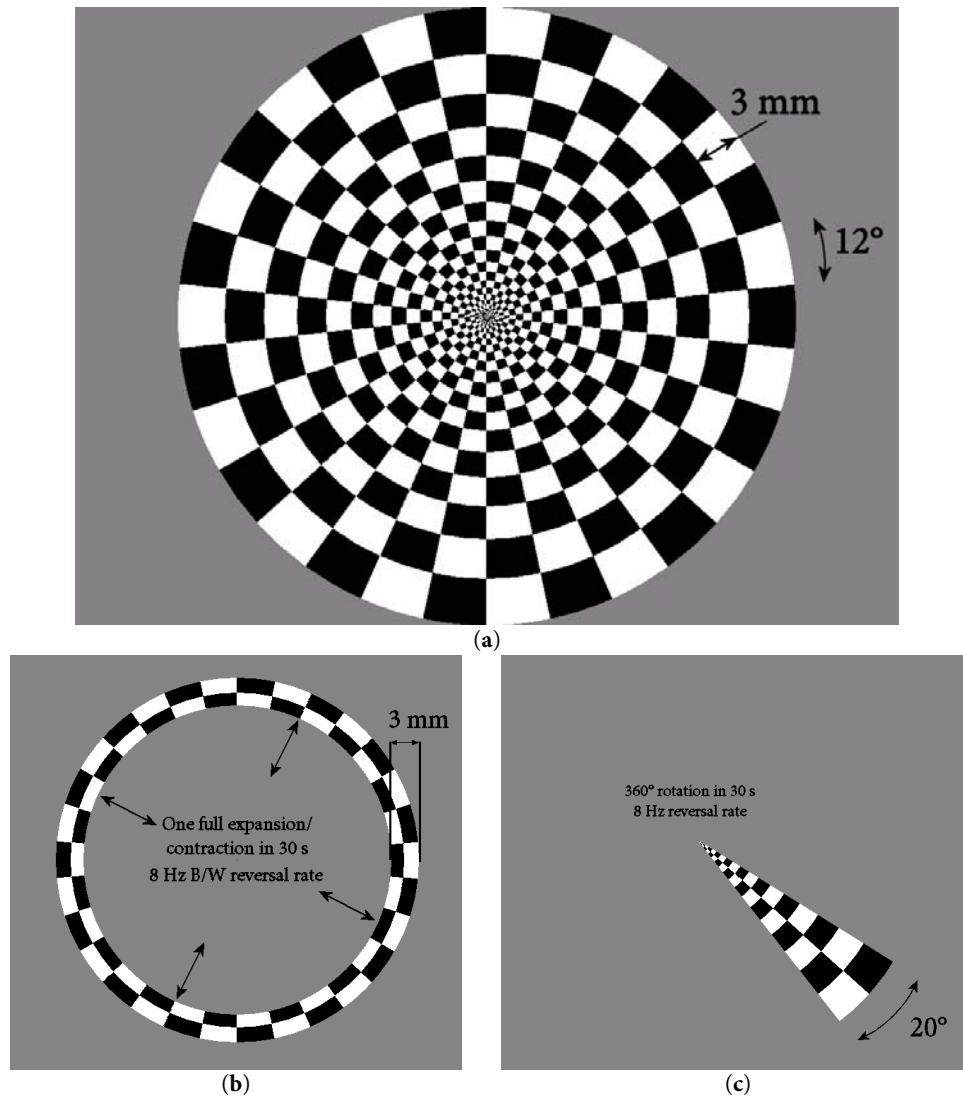


Figure 4.1a: Full field circular checkerboard. Both the eccentricity- and the polar mapping are based on this underlying stimulus. The background intensity was 50% as compared to the white checks yielding the same mean luminance as the stimulus. The red fixation point (hardly visible here) covered 1 pixel and changed colour to green at random time points (mean 4.5 s between) for 0.5 s. The checkers reversed intensity at a reversal rate of 8Hz.

Figure 4.1b: Expanding/contracting rings stimulus.

Figure 4.1c: Polar angle mapping stimulus (rotating wedge).

Eccentricity Mapping

The eccentricity mapping experiment consists of a ring expanding or contracting around a fixed point (see figure 4.1b). The minimum visual angle displayed was 0.2° . The ring was generated by copying the ring defined in transparent colour (background colour at other locations) onto the full field checkerboard stimulus using double buffering³⁰. The ring stimulus was scaled to cover 3 mm radially in the visual cortex at all times. Furthermore the radial velocity of the ring was scaled to provide an activation wave moving at approximately constant velocity in the visual cortex. The ring expanded 8 times (starting 7.5 s from the minimum display angle) during the first 4 minutes (cycle length 30 s). When the stimulus reached the edge it warped around to the middle, always stimulating 3 mm of the visual cortex in the radial direction. After the first 4 minutes the stimulus paused for 30 s while still displaying the fixation point (occasionally changing colour). For the last 4 minutes the ring contracted analogous to the first 4 minutes. The position of the ring was updated at 8 Hz to provide an almost smooth motion. In later sections radial phase will refer to phase (0 to 2π) starting from the fovea (0.2°) going to the periphery (9.2°).

Polar Mapping

The polar mapping experiment was very similar to the eccentricity mapping, only here the ring was replaced with a slice (wedge) moving clockwise the first 4 minutes starting from upper vertical (12 o'clock). One full rotation lasted 30 s. After a 30 s break moving counter-clockwise (see figure 4.1c), the activation of each area was therefore approximately 2.7 s. The wedge position was updated at 8 Hz.

Some discussion exist whether to use one or more wedges and/or rings for stimulation [75,98]. Each time excessive stimuli are added, it introduces some ambiguity in the phase determination. Assuming that left hemifield stimuli enter the right hemisphere and vice versa, the ambiguity is particularly easy to handle for two wedges placed in each of the visual hemifields. For rings or more wedges the issue is more difficult to handle [98]. To pursue the issue of using one or two wedges an experiment investigating independency between the hemispheres was done. Three conditions were shown in a block design; full field circular flickering checkerboard (1), left hemifield flickering checkerboard (2) and right hemifield flickering checkerboard (3), all reversing at 8 Hz. The three conditions were randomized (however still keeping the number of session for each stimulus type the same).

To determine if independency between the hemispheres can be assumed it is investigated if $(1) = (2) + (3)$, meaning that stimulating each hemifield separately is the same as stimulating both at once. Figure 4.2 displays the result of this experi-

³⁰ Double buffering refers to drawing to an off-screen buffer and copying the contents of the buffer to the screen at each refresh to reduce flickering.

ment, showing some interaction between the two hemifields. For this reason all stimuli in this study were produced using only one wedge and one ring. However, as the difference might not be of practical importance the stimuli design allows showing more wedges and rings by changing only a constant.

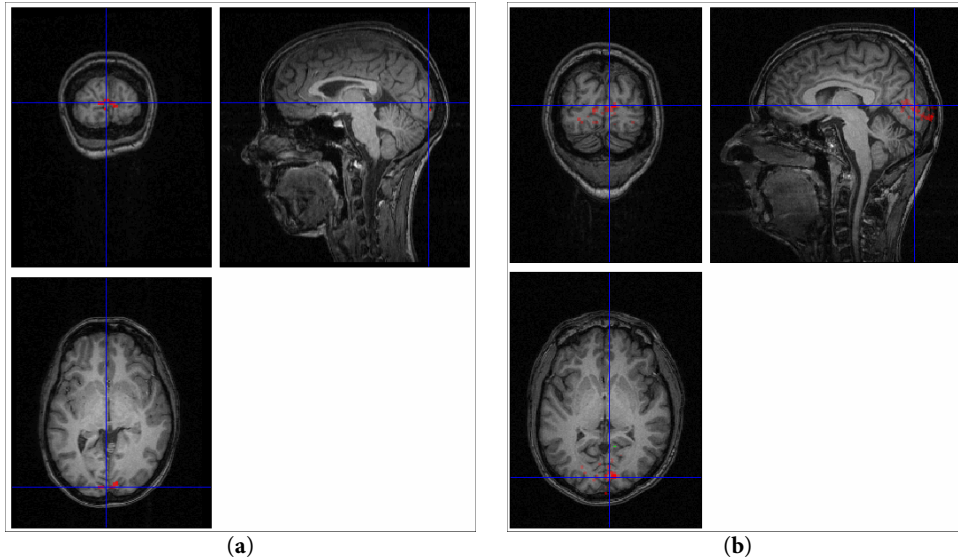


Figure 4.2: The figures show the difference between stimulating one visual hemifield at a time. Locations where the response to stimulating both hemispheres is greater than that of stimulating one at the time is shown in red, locations where the opposite is true (were there any) is shown in green. The extent is seen to be somewhat restricted to the early visual cortices (V1-V3). Figure (a) and (b) show results from two different subjects. The display of this figure is somewhat different than the others presented. The upper left picture show a COR cut, upper right show a SAG cut and finally the picture in the bottom is a TRA cut. Also the convention is neurological; this convention is standard in SPM2.

4.1.3 Scanning protocol

Data acquisition was performed using the 3.0 T MR scanner (Trio, Siemens, Erlangen, Germany) at DRCMR, Copenhagen university hospital, Hvidovre.

Ethics

The study was performed according to the Helsinki declaration. Subjects gave their informed consent. The Scientific Ethics Committee for Frederiksberg and Copenhagen Counties approved the MR protocol (journal number (KF) 01-131/03).

Anatomical Data

A structural scan was acquired using a MPAGE T₁ weighted sequence to obtain 192 slices (1 mm) with a 256x256 acquisition matrix and 256x256 mm FOV. Other parameters were: flip angle 9°, TR = 1540 ms and TE = 3.93 ms.

The scanner was equipped with the standard birdcage head coil. In addition, to test the improvement to the segmentation by the use of a surface coil array, an 8 element (MRI Devices Corp.) was used in one case.

Functional Data

An EPI GE sequence was used to obtain 26 3 mm slices (no gap) with 64x64 acquisition matrix and 192x192 mm FOV yielding a TR of 1.55 s. Slices were recorded interleaved³¹ with a 72° FA³² using a standard birdcage head coil. Subject heads were supported by the means of a vacuum cushion and foam pads to keep movement to a minimum. Motion compensation was performed at the scanner using Siemens software (PACE) [79]. 10 subjects were scanned³³.

4.1.4 Data Analysis

The images were acquired from the scanner in Dicom format from which it was converted to the format used internally in BrainVoyager.

Structural³⁴ images were corrected for inhomogeneity[92], normalized to Talairach space[78] and segmented into grey and white matter[13] to create cortical surface representations [13,24,46].

Functional images were converted to BrainVoyager format (STC). The pre-processing steps consisted of motion correction (using BrainVoyager software) followed by a slice time correction using sinc interpolation and high pass filtering

³¹ The interleaved scheme used was as follows: In case of a even number of slices the even slices was acquired first, starting from the bottom, whereas in the case of a odd number of slices the odd slices were acquired first.

³² Adjusted according to the Ernst angle (θ_E) assuming a T₁ of 1331 ms (grey matter [97]) to obtain optimal SNR. $\cos\theta_E = \exp\left(\frac{-TR}{T_1}\right)$

³³ More subjects were scanned earlier however with a slightly different paradigm due to optimization of the stimuli parameters.

³⁴ Conversion into Analyze-7 format (Mayo Clinic, <http://www.mayo.edu/bir/>) was also performed to test segmentation and bias correction using SPM2 and FSL.

(cut off: 1/128 Hz). The functional images was co-registered to the structural scan using the position information from the scanner (provided in the Dicom header) followed by a fine adjustment by maximizing the mutual information [26]. It should be noted that there might still be misalignment due to distortions in the EPI images[94].

The generally adopted method for analysis of retinotopic data is performed in the Fourier domain by determining the phase and amplitude of the frequency component defined by the cycle length [5,15,68,98].

The method directly implemented in BrainVoyager is a simple cross correlation analysis, this was the method first adopted however several limitations are present in this technique. First the method (as implemented) only allows estimation of integer lags³⁵. Secondly the simple cross correlation does not allow for inclusion of confounders in the model.

The approach used in this study relies on a GLM to perform the analysis in the time domain. This is achieved by adding sine and cosine predictors of the periods defined by the cycle length to search for periodic components in the data. This allows for inclusion of confounding predictors in the analysis, thus providing better control for aliased noise.

The resulting design matrix including 2 harmonics of the sine and cosine predictors is shown in figure 4.3, for a discussion on how many harmonics of the sine and cosine predictors to use, refer to section 4.1.5.

³⁵ A way to overcome this is to use a reference time course at higher resolution than the data and then shift it by the lag to investigate before it is resampled to the same resolution as the data.

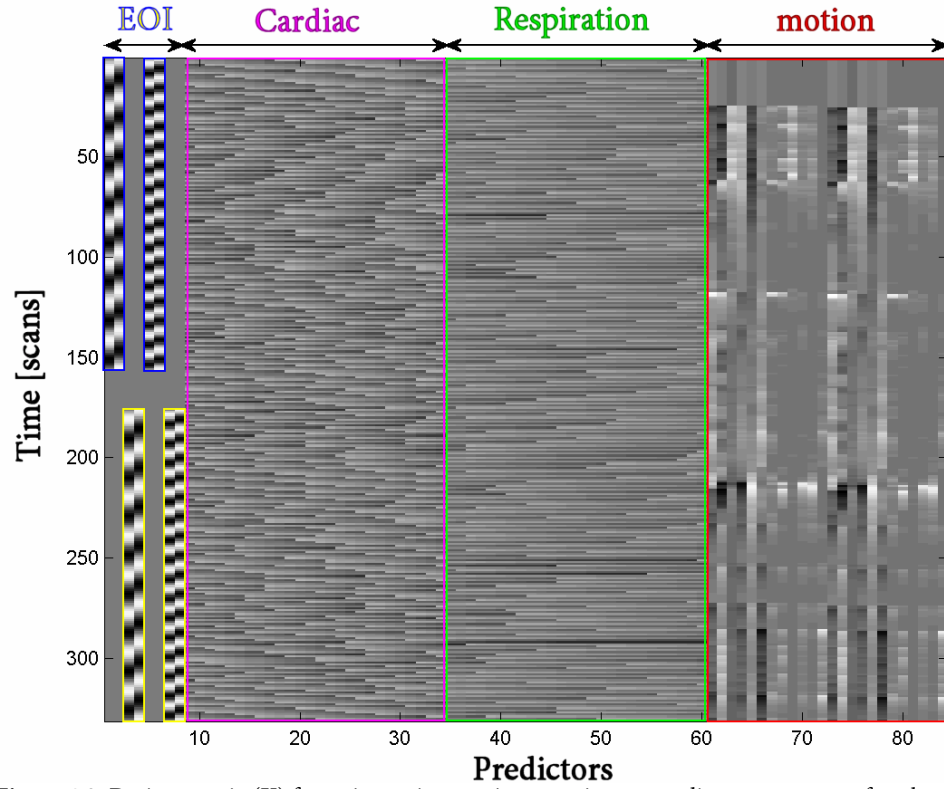


Figure 4.3: Design matrix (X) for retinotopic mapping experiment; predictors to account for physiological effects and motion have been added. The first to 8 columns are the effects of interest (EOI).

Columns 1-2: Sine and cosine predictors of frequency 1/30 Hz for the counter-clockwise run (1st harmonic, blue).
Columns 3-4: Sine and cosine predictors of frequency 1/30 Hz for the clockwise run (1st harmonic, yellow).
Columns 5-6: Sine and cosine predictors of frequency 1/15 Hz for the counter-clockwise run (2nd harmonic, blue).
Columns 7-8: Sine and cosine predictors with frequency 1/15 Hz for the clockwise run (2nd harmonic, yellow).
Columns 9-34: Predictors from cardiac cycle time course described in section 3.5.7 on page 30 (purple).
Columns 35-60: Predictors from respiration cycle time course described in section 3.5.7 on page 30 (green).
Columns 61-84: Predictors from estimated motion parameters described in section 3.4.1 on page 21 (red).

Because the spin history motion predictors proved to have only marginal effect, they were omitted from the analysis (also the use of PACE should reduce this effect significantly [79]). In cases with no significant movement (judged by visual inspection of the motion correction parameters) the remaining 12 motion predictors were also omitted. Also the response parameters from the fixation point task were included by convolving a predictor consisting of delta functions at the time of the key-presses with the HRF defined in [8] using the parameters $\tau=1.25$ and $\delta=2.5$.

As described in section 3.1.2, an estimate of β can still be found in the case of a singular design matrix by using a pseudo inverse. It should however be noted, that the estimated weight on a single predictor not orthogonal to the others is ambiguous (the solution is not unique). Correlation between confounding predictors does not cause problems because it is only necessary to estimate the effect collectively.

The covariance matrix showing the orthogonality of the design is displayed in figure 4.4.

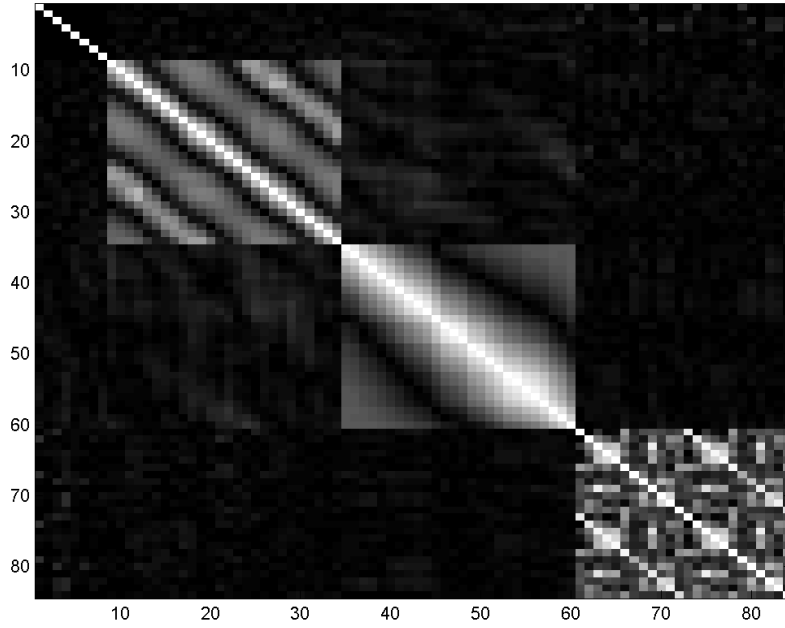


Figure 4.4: Cross correlation matrix (absolute values) of the design matrix shown in figure 4.3. White areas indicate correlation (either positive or negative). The first 8 predictors (EOI) show no mutual colinearity (sine and cosine are orthogonal); also the correlation with the remaining predictors (confounders) is negligible.

In case of correlation between EOI and the confounders, only the effects orthogonal to the confounders should be considered. This is done by projecting the confounders out of the data and estimating the β weights again, while correcting the degrees of freedom accordingly.

$\hat{\beta}_i$ can be used to reconstruct the signal \hat{Y}_i at voxel i as shown in equation (4.3) where \mathbf{c}^T is a contrast selecting the EOI.

$$\hat{Y}_i = \mathbf{c}^T \mathbf{X} \hat{\beta}_i \quad (4.3)$$

The (voxel-wise) correlation between the signal and the model is given by equation (4.4), $\sigma_i^2(\hat{Y}_i)$ denotes the variance of the reconstructed signal (EOI) and the denominator is the total variance corrected for serial autocorrelation.

$$r_i^2 = \frac{\hat{\sigma}^2(\hat{Y}_i)}{\sigma_i^2} \quad (4.4)$$

A signal to noise ratio ($\xi = \text{SNR}$ ³⁶) and a correlation coefficient (EOI) is now defined as shown in equation (4.5), where $\sigma_{e,i}$ denotes the residual error standard deviation in voxel i . This ratio is unsuitable for doing statistical test in the SPM, however it will be used to threshold the SPM.

³⁶ The signal to noise ratio is normally defined on a logarithmic (dB) scale. Here, however, it is simply the ratio between the signal amplitude and the noise amplitude.

$$\xi_i = \frac{\hat{\sigma}(\hat{\mathbf{Y}}_i)}{\hat{\sigma}_{\epsilon,i}} \quad (4.5)$$

The phase of the 1st harmonic for the reconstructed signal can be determined by using the relation given in equation (4.6) where \arctan_2 is the four-quadrant inverse tangent, $\beta_{1,i}$ is the sine predictor weight and $\beta_{2,i}$ is the cosine predictor weight.

$$\varphi_{1,i} = \arctan_2 \left(\frac{\beta_{2,i}}{\beta_{1,i}} \right) \quad (4.6)$$

An approximation of uncertainty of the phase estimate can be found by using a multivariate Taylor expansion and multiplying the standard deviation estimates³⁷. In case of more than one harmonic, another scheme must be used. In the present study the hemodynamic peak proved to be a well defined point (the wedge stimulus duration is quite short as compared to the cycle length), consequently the β weights are used to determine the peak phase analytically³⁸.

As previously mentioned, the stimuli are displayed forwards and backwards to allow estimation of the hemodynamic lag [68] by using the relation given in equation (4.7). $\varphi_{1,i}$ designates the phase estimated from the forward run and $\varphi_{2,i}$ is the phase estimated from the second run (both adjusted to be in the range from 0 to 2π).

$$\tau_i = \frac{(\varphi_{1,i} - (2\pi - \varphi_{2,i})) \bmod 2\pi}{2} \quad (4.7)$$

The resulting final phase estimate is given by equation (4.8).

$$\varphi_i = (\varphi_{1,i} - \tau_i) \bmod 2\pi \quad (4.8)$$

Obtaining this ratio for both the eccentricity mapping experiment and the polar mapping experiment gives a coordinate representation in the coordinates from the visual field ($\varphi_{i,r}, \varphi_{i,a}$) for each voxel (i).

³⁷ This is not unproblematic as \arctan_2 is restricted to $-\pi/2$ to $\pi/2$ and predictors are measured both clockwise and counter-clockwise (including the last one should decrease the standard deviation).

³⁸ In practice this was accomplished by using a more densely sampled predictor to reconstruct the signal and locate the maximum value. Thus being a little more computationally demanding this solution works for arbitrary no. of harmonics.

4.1.5 Results

How many harmonics?

The following is concerned with the shape of the hemodynamic response. The analysis method suggested does not imply any other shape to the hemodynamic response than the periodicity, therefore a verification of actual fitted response is desirable. A voxel with representative SNR ($\xi=1.1$) was used as an example in figure 4.5 where the MR signal along with the reconstructed signal from the GLM is plotted. The corresponding averaged signal over the first 8 cycles is shown in figure 4.6.

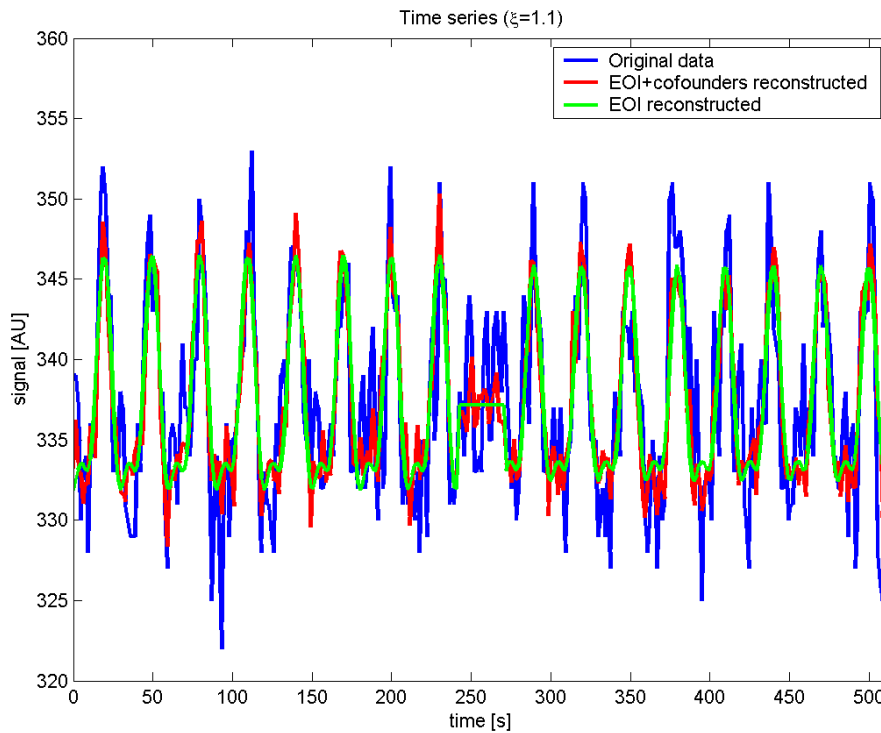


Figure 4.5: Signal in voxel with $\xi=1.1$. The original signal (after pre-processing) is shown in blue, the reconstructed signal using all predictors (including confounders) is shown in red and finally the signal reconstructed using the effects of interest is shown in green. The number of harmonics was 2. It is seen that the reconstructed signal corresponds quite well to the measured.

As a remark it can be noted that the SNR would have been (wrongly) estimated at $\xi=1.4$ if serial autocorrelation had not been considered.

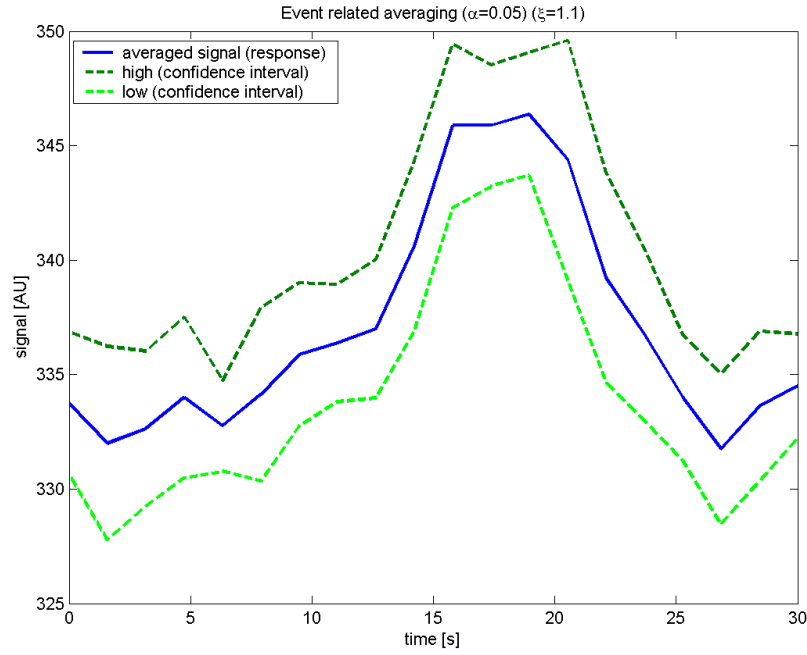


Figure 4.6: Event related averaging. The signal was first divided into 8 parts (events) corresponding to the CCW run of the polar mapping experiment. Because of jittering the signal is not acquired at the same time in each event therefore linear interpolation is done in the time series to obtain 8 values for each of the (approximately) 20 samples. The 8 values are then averaged and an estimate of the variance is obtained, used to construct the confidence interval (using standard t-statistics). The confidence interval shown is created using $\alpha=0.05$ (type I error). The maximum signal change as compared to the average value with the EOI subtracted was 2.9%.

To investigate how the number of harmonics changes the reconstructed signal from 1 to 7 harmonics was used as illustrated in figure 4.7. Adding more than 2 harmonics only has little effect and as previously shown in figure 4.5 the fit with 2 or in fact also 1 harmonic is very good.

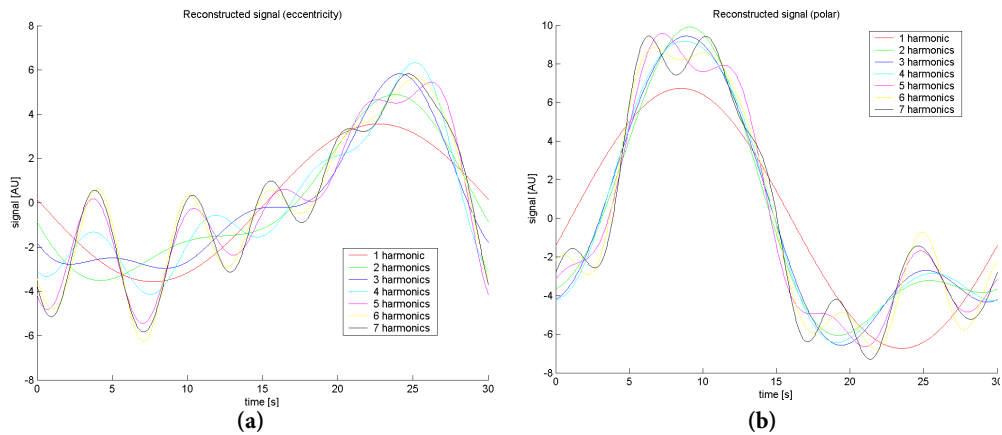


Figure 4.7: Effect of adding harmonics. Figure (a) shows the reconstructed signal using the EOI (at higher resolution) from the eccentricity mapping experiment. Figure (b) shows the same (the same voxel) for the polar mapping experiment. Note that this is not the same voxel as in figure 4.5 and figure 4.6, however the SNR is the same ($\xi=1.1$). The maximum signal change is also 2.9% in this case.

Another way to investigate if an analysis method is appropriate is to investigate the estimated hemodynamic lag. Figure 4.8 illustrate the reconstructed signal using 1 and 5 harmonics for the clockwise and the counter-clockwise run. It is seen that changing the number of harmonics might influence the estimated phase however in cases where the function has a broad peak adding more harmonics does not improve the localization of the peak value. The number of harmonics used in the following will be two because this provides a reasonable fit to the observed signal (see figure 4.5).

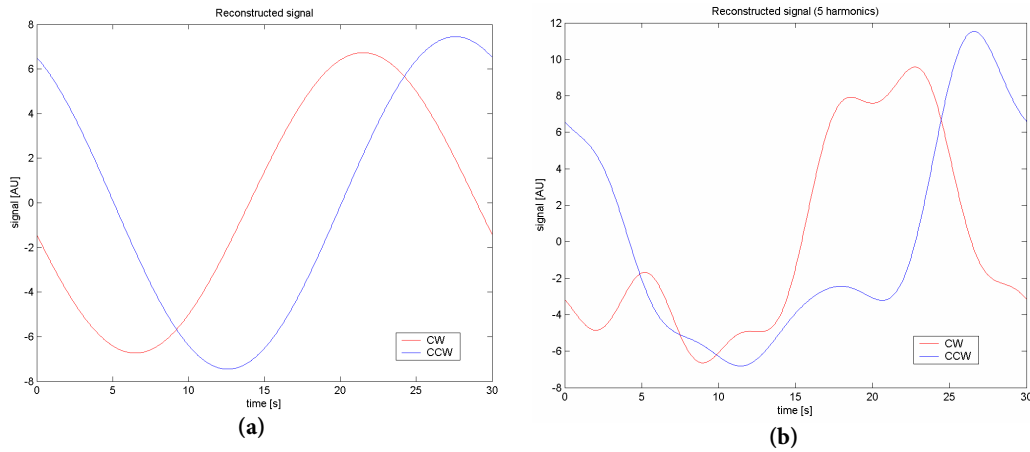


Figure 4.8: Changing the number of harmonics from 1 (a) to 5 (b) changes the estimated hemodynamic lag from 3.1 s to 2.1 s. The red graph is the phase estimated from the CW run (2. run) whereas the blue graph is the estimated phase from the first run subtracted from 2π (CW is considered positive due to technical reason in the way BrainVoyager represents lags). The estimated hemodynamic lag is the difference between the arrivals of the two responses. This estimation is always based on the maximum value of the reconstructed signal. The SNR (ξ) of the voxel considered was 0.9.

The findings displayed in this section were also found to be consistent with other voxels with SNR higher than 0.7.

Hemodynamic lag

Figure 4.9 shows the hemodynamic lag estimate for all voxels scanned. The same map averaged over 4 runs (2 x polar, 2 x eccentricity) can be seen in figure 4.10. This method for estimating the hemodynamic delay was used in a study by Sereno in a pioneer article on retinotopic mapping [68]. However, the experiment was not used to investigate the spatial distribution of hemodynamic lags. Because the BOLD signal is based on blood delivery, spatial differences might arise due to varying distances to arteries as investigated by [44].

The two scatter plots (figure 4.9 and figure 4.10) indicate that the true hemodynamic lag in the primary visual cortex is actually closer to 4 s than the 5 s sug-

gested³⁹ by the canonical HRF in SPM2 (see figure 2.9). This result is also somewhat in conflict with hemodynamic lags of 6-10 s reported by Gössl et al. [35].

The corresponding spatial distribution of lags is seen in figure 4.11 .

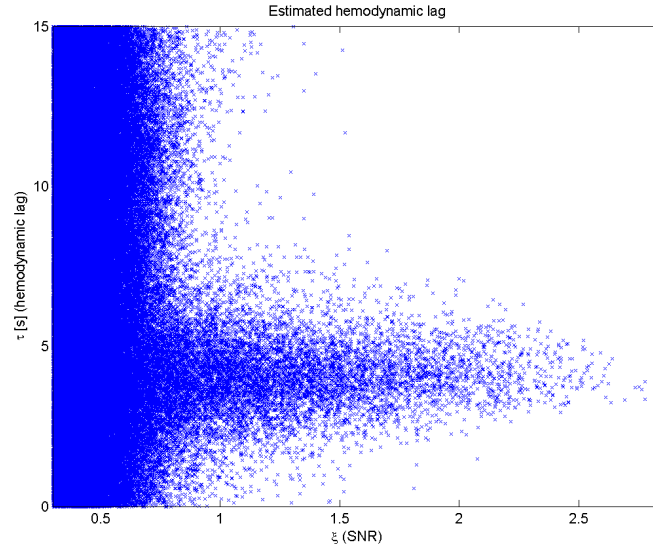


Figure 4.9: Estimated hemodynamic lag. Each cross denotes a voxel. The lag is found to be quite well defined for voxels with $\xi > 1$. For $\xi < 1$ the lag assemble noise justifying the use of ξ for thresholding to some extent. The mean hemodynamic lag for voxels with $\xi > 1$ is 4.2 s and standard deviation 1.5s.

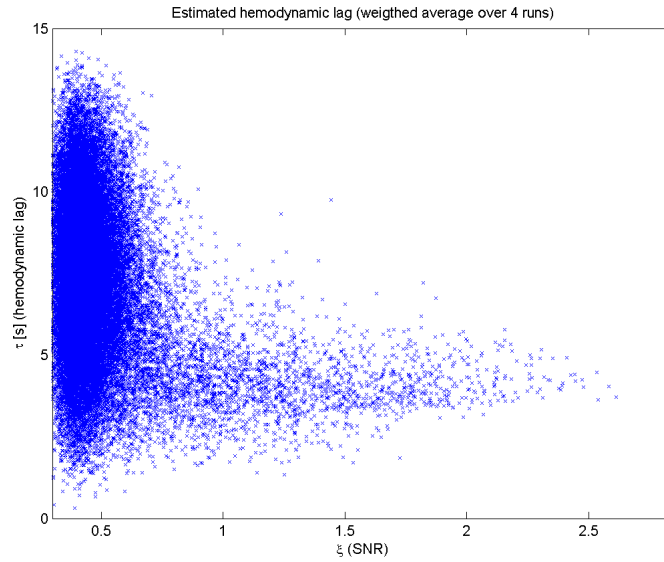


Figure 4.10: Weighted average of estimated hemodynamic lag. This figure is the equivalent of figure 4.9, but averaged over 4 runs. This is seen to reduce the variance slightly. The ξ is now the average over the 4 runs, each of the runs were thresholded at $\xi = 0.47$ before averaging. The mean value for voxels with $\xi > 1$ is still 4.2 s, however, the variance is now (naturally) reduced to 0.2 s.

³⁹ A standard t-test does not apply here because the observations (voxels) are not independent.

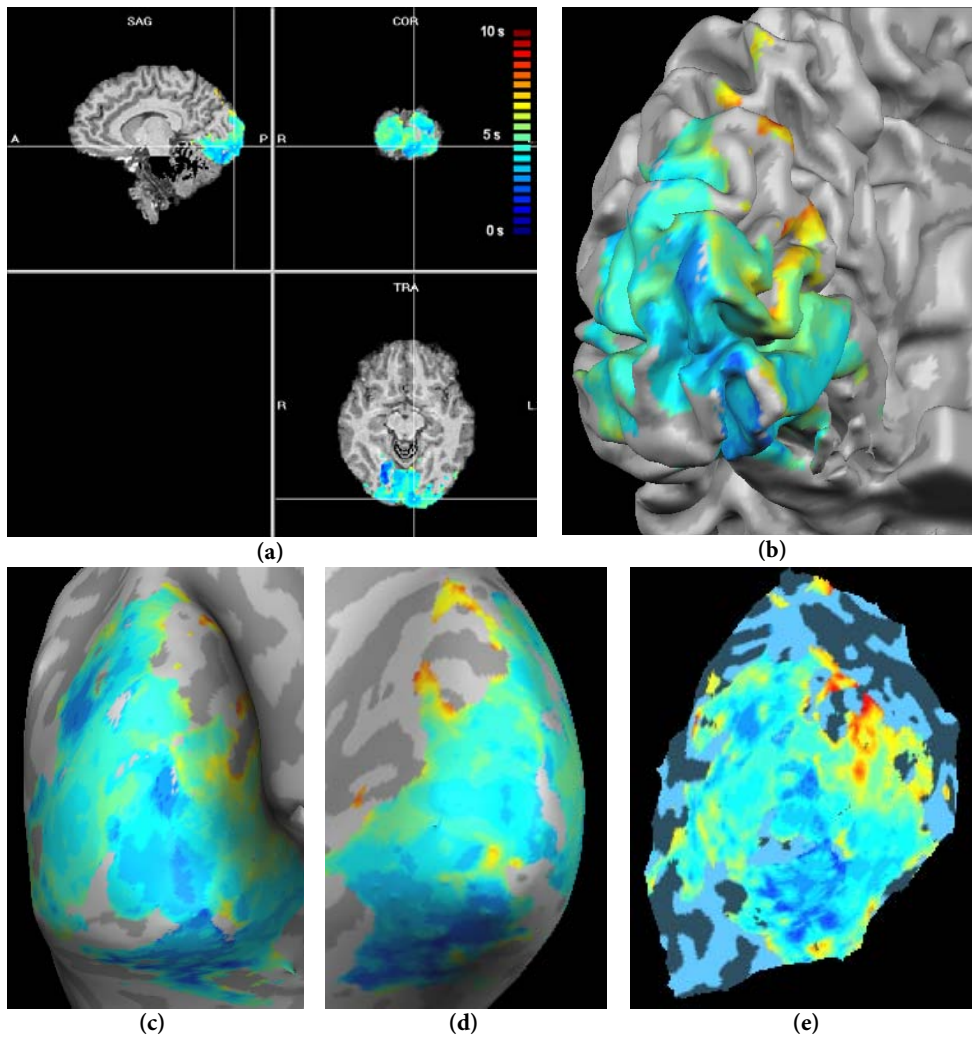


Figure 4.11: Spatial distribution of hemodynamic lag (time to peak).

In (a) the activation is overlaid on the structural scan.

(b) shows the lag overlaid on a folded representation of the cortical surface of the left hemisphere (dilated and smoothed GM/WM surface).

(c) and (d) show inflated versions of left and right hemispheres respectively, with overlaid hemodynamic lag.

The view shown in figure (e) is an unfolded view of the right hemisphere, only the occipital cortex has been unfolded allowing the unfolding to be done without defining cuts. This method requires manual definition of the region of interest and unfolding vectors and is thus very time consuming.

All hemodynamic lags are in the same colour scale from 0 to 5 s (shown in (a)). The GLM was fitted using 5 harmonics.

Independent Components

In order to further investigate the BOLD response in the retinotopic mapping experiments spatial ICA was performed on the data (after the pre-processing steps had been performed). To reduce the input data analysis was restricted to the cortex, using a mask constructed from the unfolded representation of the cortex. Voxels 1 mm on the inside and 2 mm outside of the smoothed and dilated WM/GM surface was included in the mask. Furthermore, the input dimensionality was reduced to 30 by using SVD to perform PCA, from the resulting data 30 components was extracted using the FastICA algorithm [43]. The components were sorted according to the root mean square (RMS) of the dataset reconstructed using only the specific component.

Figure 4.12 shows 5 selected components from the polar mapping experiment and the corresponding maps. The maps were thresholded using the z-scores method as described by McKeown et al. [54]. The first component is expected to describe activation related to the key-press. The Talairach coordinate of highest z-score was $(x, y, z) = (-45, -8, 46)$, this is in the neighbourhood of Brodmann area 4 (primary motor cortex). However, this is quite uncertain as the time series does not seem to be directly related to the task. Also the activation found using the response predictor from the GLM produced similar maps. The time series of the next four components is seen to have peaks at 1/30 Hz and 1/60 corresponding to 1st and 2nd harmonic of the visual stimuli. This also provides a strong argument that two harmonics is sufficient to capture the dynamics of the BOLD response. The remaining 25 components did not have time series or maps related to the stimuli, rather some seemed to be related to movement or physiological noise.

Similar results from the eccentricity mapping experiment are shown in figure 4.13, the merged map of the two components show that the components are restricted to the visual cortex. Results obtained from other subjects (data not shown) were similar.

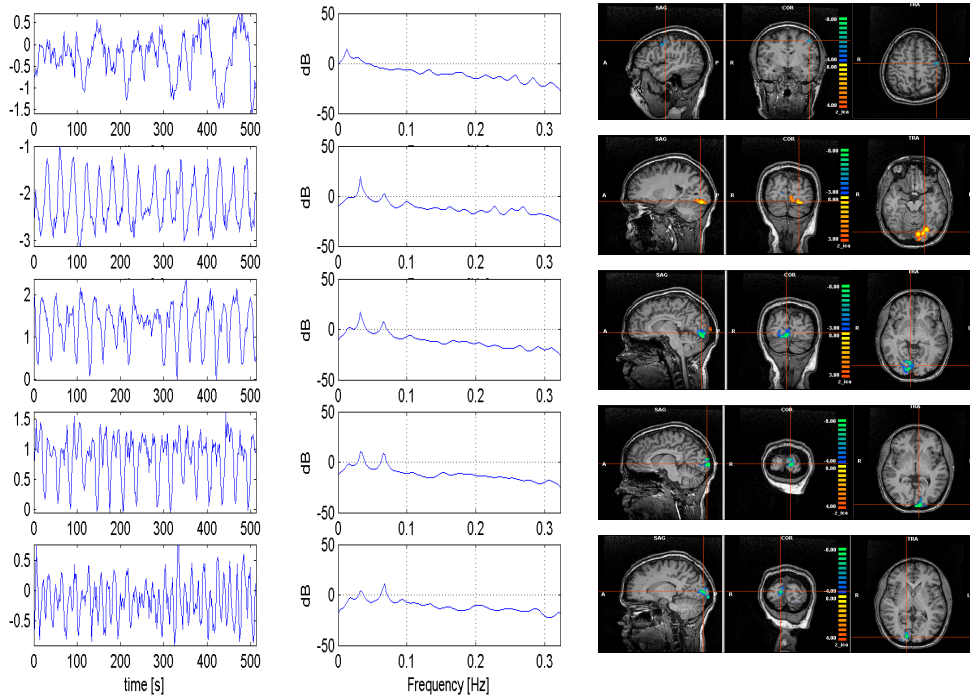


Figure 4.12: Selected independent components for polar mapping experiment. The 5 rows correspond to each their (spatial) independent component. The first column show the time series (signal in AU) the second column the Yule-Walker power spectrum density (32nd AR model, 256 Fourier components, mean was subtracted). The last column shows the corresponding maps in an isometric view. Note that the signs of the components are arbitrary.

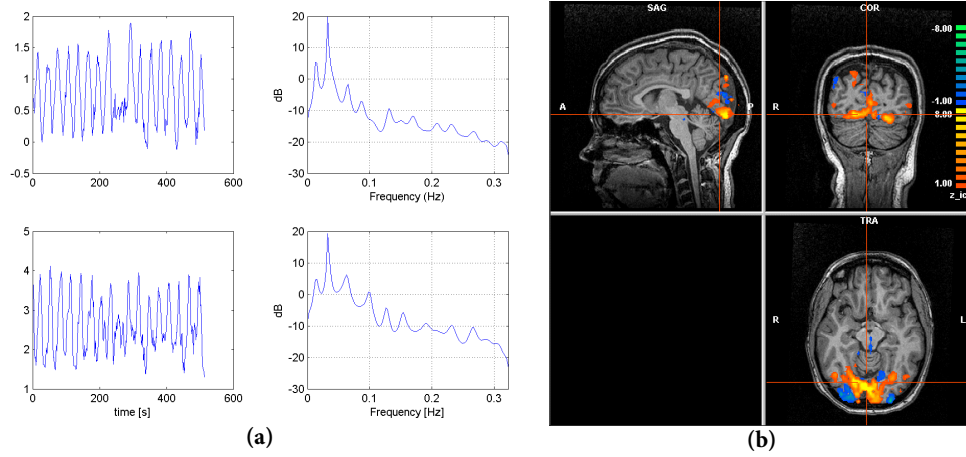


Figure 4.13: Independent components for eccentricity mapping experiment. Figure (a) shows two components showing agreement with the visual stimuli (note that the components appear as a sine and cosine wave). Also the power spectrum (same parameter as in figure 4.12) is shown. Figure (b) shows the merged map of the two components (colouring is based on the z-score).

Retinotopic maps

Figure 4.14 shows the estimated phases from the eccentricity mapping experiment and figure 4.15 shows similar results from the polar mapping experiment. The isometric views proved very consistent over subjects however the surface representation showed to be very dependent on the co-registration between the structural and the functional scan. Also the segmentation has great impact on the results. In order to provide a good surface representation time consuming manual editing of both co-registration and segmentation proved necessary.

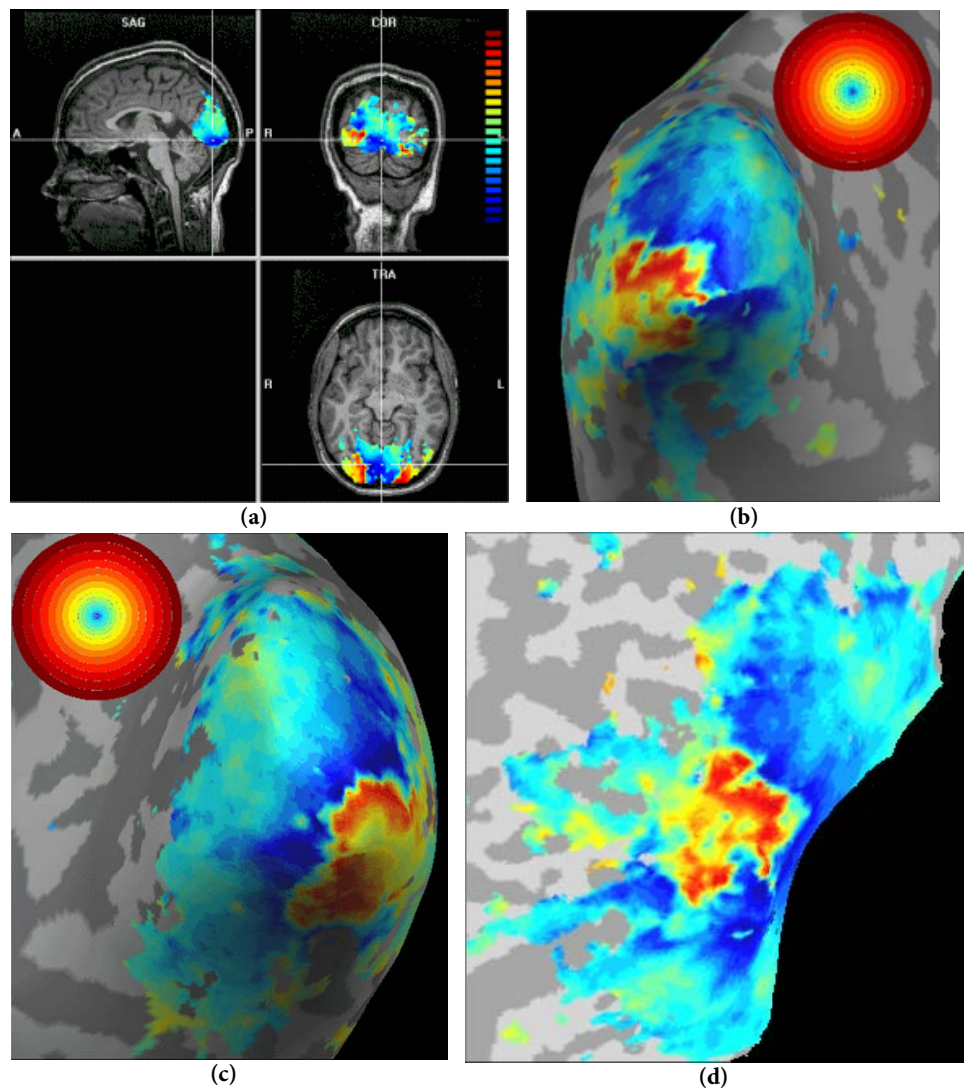


Figure 4.14: Phases from eccentricity mapping experiment. Figure (a) shows an isometric view. (b) and (c) are inflated versions of the left and right hemispheres. Finally figure (d) show a standard unfolded view of the left hemisphere. The colour map is the same for all the 4 figures and voxels having $\xi > 0.7$ are considered active. The functional overlays have been interpolated linearly to match the $1 \times 1 \times 1$ mm resolution of the structural scan, other than this no smoothing has been applied.

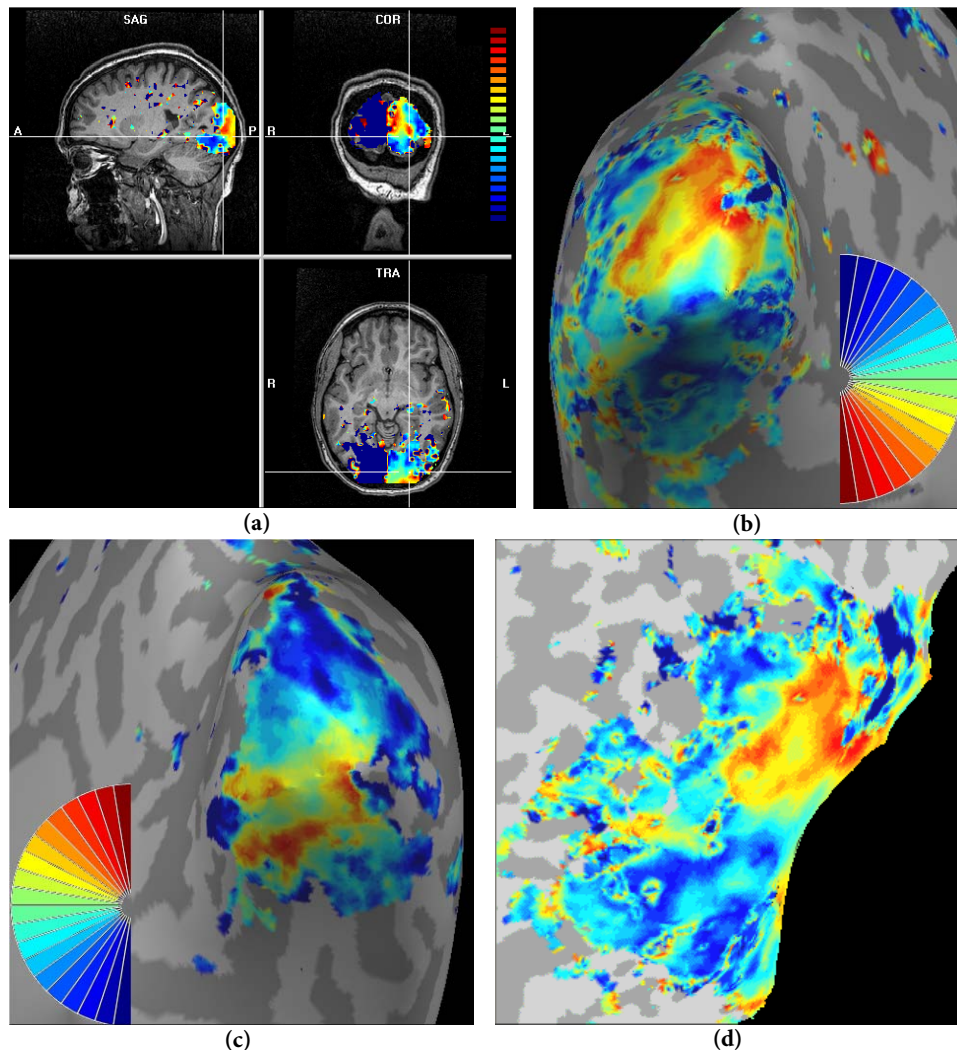


Figure 4.15: Phases from polar mapping experiment. Figure (a) shows an isometric view. Due to the limited number of overlay colours possible in BrainVoyager, only phases for the left hemisphere is shown (all the phases larger than π are set to zero). It is seen that visual input from the right visual hemifield is almost completely restricted to the left hemisphere (phases up to π). This is exactly what is expected and provides a strong argument that the analysis is quite robust. (b) and (c) are inflated versions of the left and right hemispheres. Finally figure (d) shows a standard unfolded view of the left hemisphere. The colour map is the same for all the 4 figures and voxels having $\xi > 0.7$ are considered active. The functional overlays have been interpolated linearly to match the $1 \times 1 \times 1$ mm resolution of the structural scan, other than this no smoothing has been applied.

The VFS map computation relies on local gradients on the unfolded surface and is therefore extremely vulnerable to noise and misalignment between the structural and the functional scan. To address problems related to noise in the surface phase maps a smoothing was applied before calculation of the visual field sign maps⁴⁰. Calculations of the VFS before smoothing reveal maps looking completely random. The resulting map is shown for one subject in figure 4.16. Although not

⁴⁰ Using a 5 mm standard deviation Gaussian filter as implemented in BrainVoyager.

completely convincing the maps are actually comparable and consistent with the literature [75]. To limit the extent of this section only a set of images from one subject is shown.

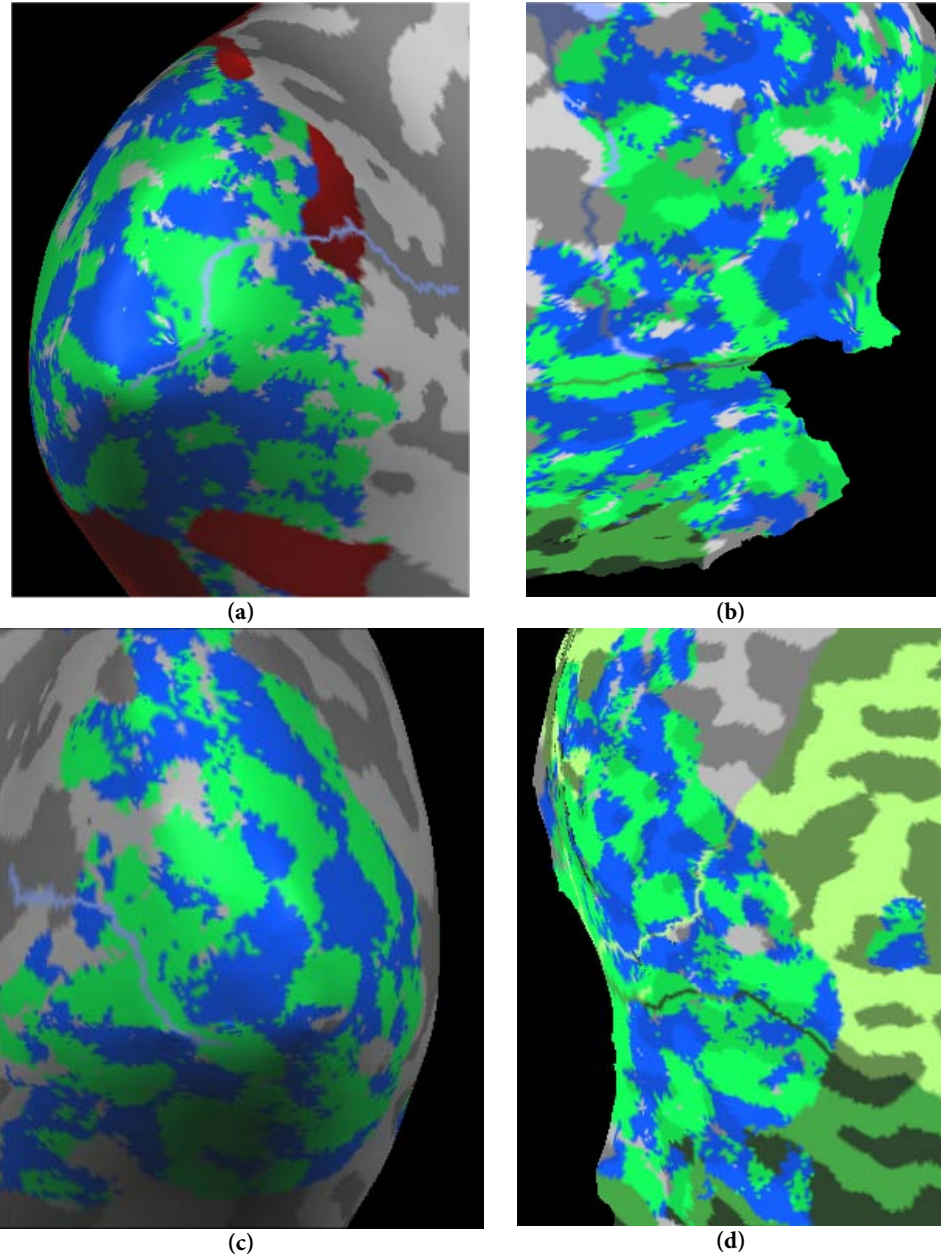


Figure 4.16: Visual Field Sign maps. Figure (a) shows the VFS map for an inflated version of the left hemisphere, the thin blue line denotes the CS. Figure (b) shows an unfolded version based on a cut along the CS, the map is only partly corrected for distortions to reveal the location of the cut. Figure (c) shows an inflated view of the right hemisphere with the CS marked. Figure (d) shows the unfolded and distortion corrected (to 14% linear distortion) version of the right hemisphere. Areas with negative VFS (mirror image representation) is shown in green, whereas areas with positive VFS is blue. V1 has negative VFS and is expected to be placed on both sides of the CS (upper visual field go to the lower part of V1 and vice versa). V2 has positive VFS and V3 have negative VFS. Visual areas higher than this usually does not provide good mapping results using VFS maps [75,98].

Perimetry

Having obtained the mapping from the visual field to the cortex other investigations are also possible. One example presented here is a method to do perimetry by back projecting the activation to the visual field. This type of investigation was suggested by Morland et al. [56], but reproducibility does not seem to have been investigated.

The general idea is simply to plot each combination of detected phases ($\phi_\omega \phi_r$) on a representation of the visual field, consistent with the method used in multifocal Visual Evoked Potential (VEP) studies [40]. This map is bound to be very vulnerable to noise and the threshold selected. Noise is expected to occur in random phases and therefore spread all over the visual field causing difficulties in localization of possible scotomas⁴¹. Because the visual field is represented more densely in the cortex at low eccentricities this type of visualization does not provide the optimal information and thus other methods should be considered.

It should also be noted that this technique needs to be investigated further in relation to reproducibility and consistency both on normal subjects and subjects known to have scotomas⁴².

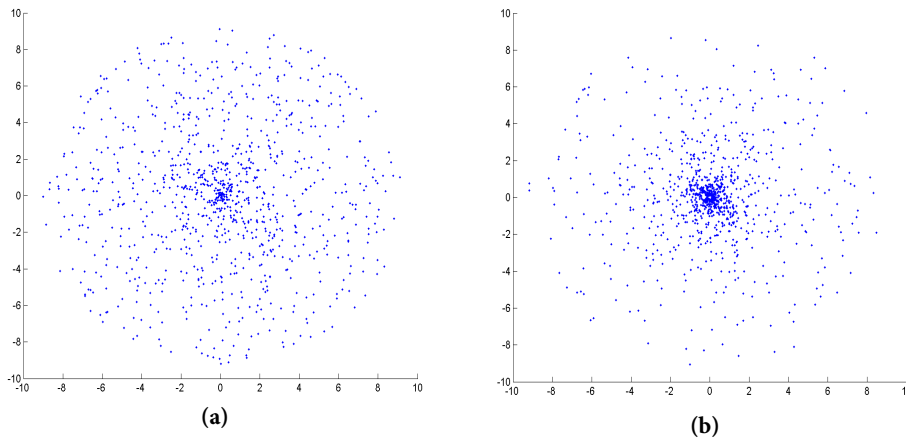


Figure 4.17: Perimetry. Figure (a) shows the activation back projected to the visual field each blue dot represents a voxel (only voxels with $\xi > 0.7$ were considered). The figure is a linear display of the phases in the radial direction meaning that the figure does not represent the visual field (it has been scaled with the cortical magnification). This figure should optimally provide the same activation for all radii, which is approximately the case (verified by plotting histograms of the phases). Figure (b) shows the same backprojection however taking the cortical magnification into account more activated voxels are (naturally) seen near the fovea. This illustrates that another representation of the visual field (such as a 3 dimensional histogram) would clearly be preferred.

⁴¹ Area of diminished vision within the visual field.

⁴² The method should also be compared to other means of visual field testing such as multifocal VEP.

4.2 Stereo Vision

The following section describes an experiment intended to investigate response to disparity/stereo visual input (different stimuli on each eye). To display different stimuli on each eye, two screens would normally be needed. However, using a technique known as colour coded 3-D makes it possible by using a combination of coloured glass in front of the subjects eyes [39]. An affine transformation of two images recorded with displaced cameras is used to form the final image. The method is adopted from [39] and implemented by Per Skafte Hansen, Danish Bankers' Association.

4.2.1 Experimental Setup and Data Acquisition

The experimental setup is very similar to the one described in retinotopic mapping experiment, the only difference being that the subjects viewed the screen through a set of magenta/olive coloured spectacles.

4.2.2 Visual Stimuli

A total of 11 different colour coded images were shown as illustrated in figure 4.18. Changing the visual stimuli from non-stereo to colour coded 3-D changes the colours in the image – therefore a response simply due to differences in colour would be expected. To minimize this effect the 3-D effect was added gradually by simply alpha blending the registered 3-D image onto the original non 3-D image. The gradual change to 3-D was linear ($\alpha = 0$ to 1) and occurred over 18⁴³ steps, each step lasting 0.15 s. The final image ($\alpha = 1$) was shown for 3 s followed by a gradual change back to non 3-D over 5 s (over 8 steps).

Each image existed in four versions: A normal colour version, a colour coded 3-D version, a black and white version and a black and white version with colour coded 3-D effect. These images were shown in a randomized event related paradigm each image being shown 7 times. In addition, to add randomization 14 null events were introduced (images displayed without adding 3-D effect). Further randomization was introduced by incorporating a variable break before the beginning of the gradual change to 3-D. The break time was drawn randomly from a list of values with mean 1.7 s and standard deviation 1.0 s. The paradigm lasted approximately 19 minutes.

The subjects were told to report (by pressing their right hand index finger) when they experienced an increased feeling of depth in the image. Pressing a button is known to produce activation in both the motor and sensory areas. However, the

⁴³ The 18 steps are the intermediate giving a total of 20 steps.

region of interest (visual cortices) is quite far away from these activation areas and therefore the task should not pose a problem [14,37]. This paradigm was also implemented in E-Prime (Psychology Software Tools, Pittsburgh, USA).

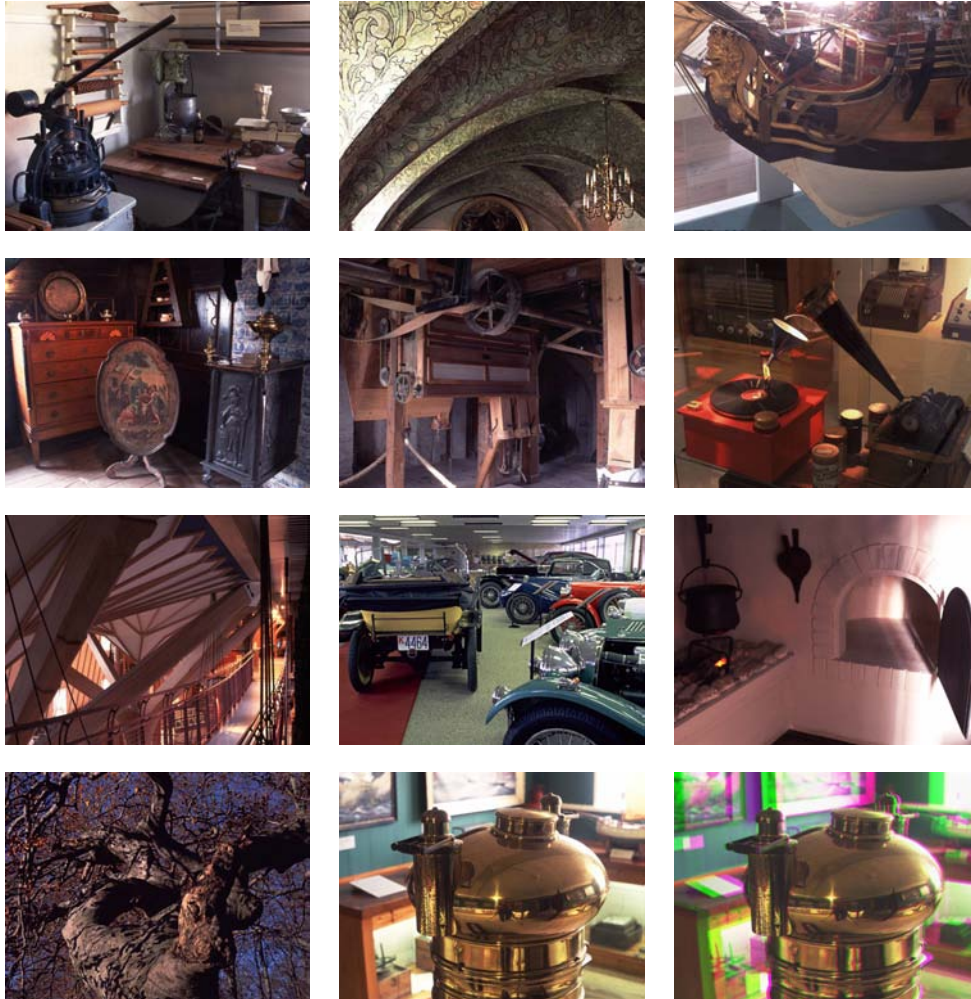


Figure 4.18: The 11 colour coded images. The image in the lower right corner is shown in the colour coded 3-D version of the image just to the left of it.

4.2.3 Data Acquisition

The scanning protocol was identical to the one used for retinotopic mapping however 40 slices were acquired to obtain full brain coverage resulting in a TR of 2.37 seconds. A total of 477 volumes were recorded.

4.2.4 Data Analysis

Pre-processing steps are identical to the retinotopic mapping experiment.

The analysis was performed by using a GLM with the predictors corresponding to the time of the key-press⁴⁴ convolved with the HRF defined in [8] using the parameters $\tau=1.25$ and $\delta=2.5$. Unfortunately, the physiological recordings were lost due to hardware malfunction and therefore these parameters could not be included in the GLM.

4.2.5 Results

Only one subject was scanned with both the retinotopic mapping paradigm and stereovision. Unfortunately the quality of the scan did not allow for a good delimitation of the visual borders the result show are therefore highly preliminary.

The following shows the activation observed from at the time of the keypress activity believed to be related to the key-press (although more anterior than expected) is seen in the left hemisphere as expected. The activation is seen to be restricted primarily to secondary visual cortices. However as delimitation of the visual borders were not possible any conclusive statements to which areas are activated cannot be given. Table 4.1 show activation sites (of maximum t-values) with the related Brodmann areas (BA). The activation in BA 19 is denoted V5/MT based on coordinates found by Friston et al. [27]. Coordinates in BA 18 are believed to be part of V3 or V4. Exact localization is not possible without delimitation of the visual borders because of the possible displacements between subject according to [17]. However, the coordinates is in agreement with activation in the occipital lobe found by Beer et al. 2002 during a movement related task and supports the proposal that the area is related to perception of optical displacements at different depths (3-D vision) [7].

⁴⁴ In case of key-presses at times with no 3-D effect present these event was removed (however no such events were present). Also events where the subject (accidentally) had pressed more than one button or the same button twice were regarded as one event.

Versions with events separated into colour and black/white events were also tried, however, no difference between the two event types was detected.

The activation of BA area 40, 41, 42 and 44 is believed to be related to the response task (motion and judgement of 3-D perception), as these areas are close to the primary motor and sensory areas.

Table 4.1: Stereo vision. Coordinates of maximum t-values found during the stereovision paradigm. Coordinates are Talairach coordinates in mm [78]. Labelling BA was done using the Talairach demon [48]. A t-value of 3.0 corresponds to $p=0.05$ (FDR).

t (475 degrees of freedom)	Talairach coordinate (x, y, z)	Description
8.551	-62, -7, 10	Left temporal lobe, BA 42
7.872	47, -71, -11	Right occipital lobe, secondary visual area, BA 19 (V5/MT)
7.256	-53, -30, 40	Left Parietal Lobe, BA 40
6.535	-52, -17, 14	Left Temporal Lobe, BA 41
6.174	-51, -74, -8	Left occipital lobe, secondary visual area, BA 19 (V5/MT)
6.096	-52, -30, 39	Left temporal lobe, BA 40
5.708	-35, -91, 1	Left occipital lobe, secondary visual area, BA 18
5.427	-54, 14, 10	Left temporal lobe, BA 44
4.851	53, 13, 8	Right frontal lobe, BA 44
4.95	11, -85, -7	Right occipital lobe, secondary visual area, BA 18

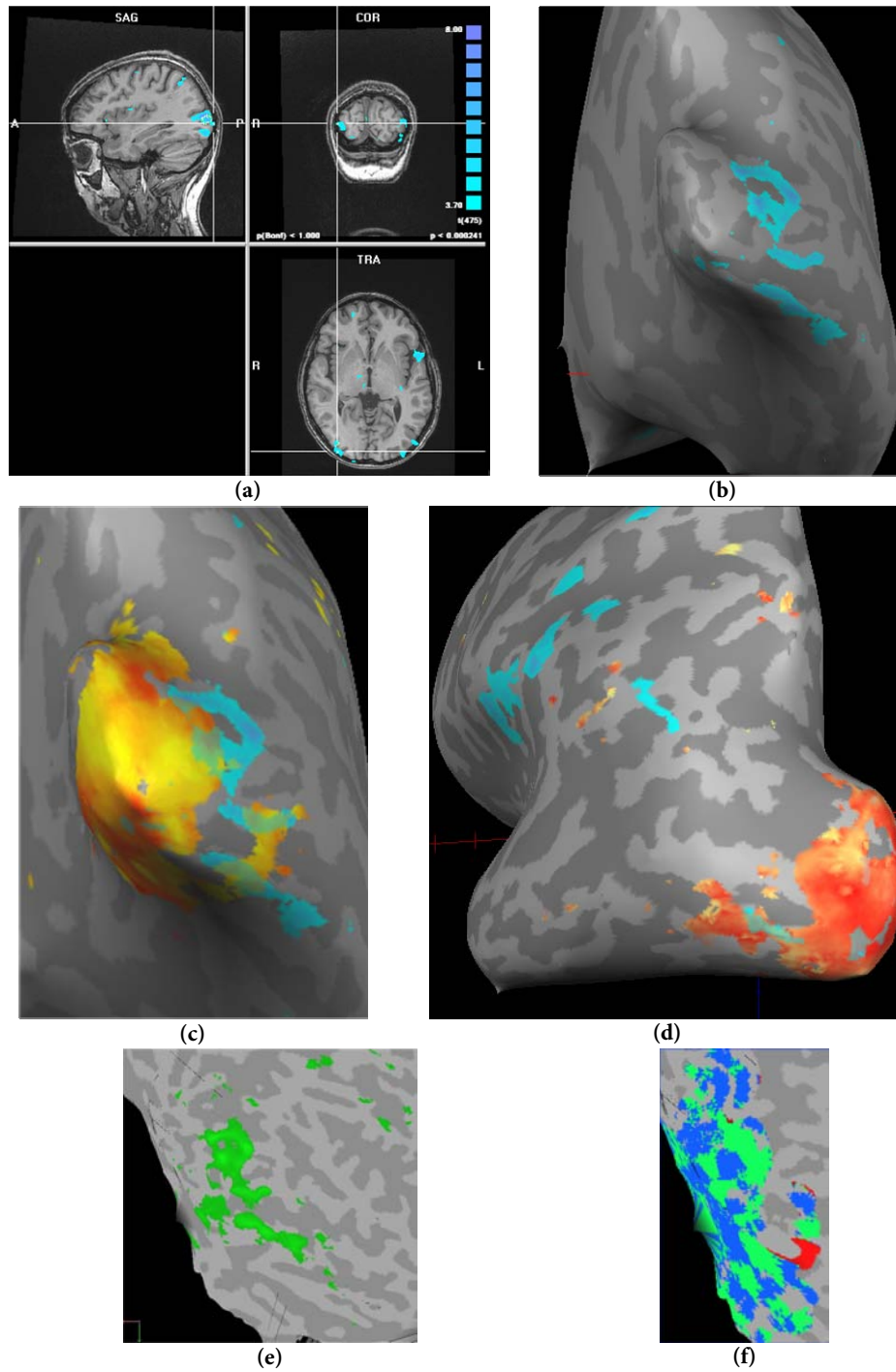


Figure 4.19: Stereo vision. Figure (a) shows the activation in a isometric view. Figure (b) shows the activation in the right hemisphere as an inflated view activation is seen primarily in what is expected to be higher visual cortices (V3 and higher). This is further illustrated in figure (c) where the activation from the polar mapping (yellow-red confirms to lower right-upper right visual field). A similar of the left hemisphere is shown in figure (d), note the activation in the more anterior part believed to be caused by motor activity (key-press). Figure (e) shows an unfolded view (right hemisphere) due to errors in segmentation the view is quite distorted. An attempt to visualize the field sign map although appropriate for delimitation of the visual borders is seen in figure (f). In all the figures voxels exceeding a threshold of $p=0.01$ (FDR) was considered active.

4.3 V5-V1 Back Projection

This experiment was provided by Professor, dr. phil. Axel Larsen, department of psychology, University of Copenhagen (KU). Only the basic idea of the study (enough to motivate it) will be presented. The experiment aims to prove the existence of back projections from V5/MT (motor area in the visual cortex) to the primary visual cortex (V1). The general hypothesis is that activation in V1 is needed for visual awareness, as suggested in [62]. The paradigm exploits the concept of imaging or apparent motion (AM). If two visual stimuli are shown sufficiently close to each other both temporally and spatially the actual perception is not two distinct events but rather a motion from one point to another.

4.3.1 Experimental Setup

The experimental setup and data acquisition is identical to the one described in section 4.1. The only difference was that the number of acquired images in this study was 485, each consisting of 26 slices.

4.3.2 Visual Stimuli

The visual stimuli are presented in a standard block design without randomization. The stimuli consist of 4 different block types and one baseline block. Each block lasted 15 s including the baseline yielding a frequency of each block of 1/75Hz fast enough to avoid collision with the high pass filter. The blocks/conditions were as follows:

0. Baseline
1. Apparent motion (AM)
2. Flashing bars (FB)
3. Real motion (RM)
4. Flashing dots (FD)

A red one pixel fixation point was shown in the middle of the visual field at all times (including baseline). Subjects were informed to keep their focus on the fixation point at all times but no explicit control task was implemented.

The first condition (AM) consisted of four dots as shown in figure 4.20a. The two dots denoted 1 was displayed (400 ms blink) followed shortly by the dots denoted 2 (400 ms blink) to create an apparent motion effect. This cycle rate of 800 ms was identical in all the following conditions.

In the FB condition two bars connecting the dots (1-2) from AM are shown. The time to show the bars was scaled to provide equal mean luminance as the other conditions (see figure 4.20b).

In the RM condition (figure 4.20c) the dot moved as smoothly as the refresh rate of the screen (60 Hz) between 1-2 (both forwards and backwards).

The last condition FD (figure 4.20d) consisted of dots at all four points simply blinking on and off (400 ms on, 400 ms off).

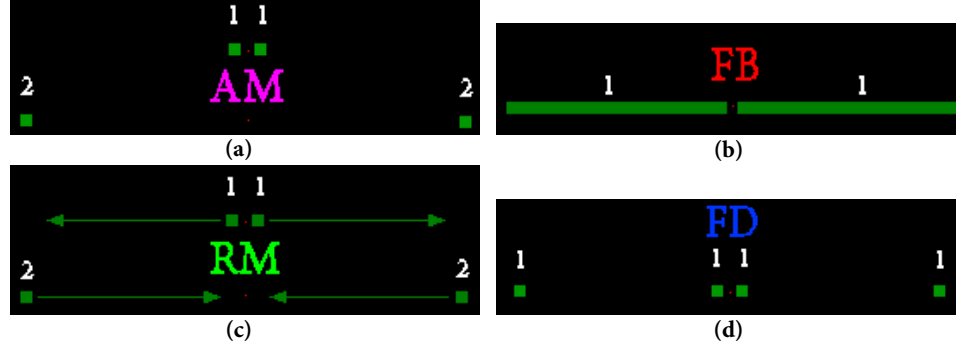


Figure 4.20: Visual stimuli for V5-V1 backprojection paradigm. The two inner rectangles (denoted 1 in figure (a)) are shown 7 pixels off center and the distance between the rectangles inner and outer rectangle (denoted 2 in figure (a)) is 120 pixels. This corresponds to an eccentricities of 0.2° and 3.1° respectively (or $\phi_r = 0$ rad and $\phi_r = 1.2$ rad).

4.3.3 Data Analysis

Pre-processing steps are identical to the ones described earlier.

A predictor was formed for each of the 4 conditions by convolving a vector describing the block design (value 1 during the block and 0 at other times) with the HRF defined in [8] using the parameters $\tau=1.25$ and $\delta=2.5$. Physiological predictors were added along with movement predictors where appropriate (judged by visual inspection of the motion correction time series).

4.3.4 Results

5 different contrasts were constructed to allow visualization of the conditions. One for each conditions and one showing areas more activated by the AM condition than by the FD condition ($[1 \ 0 \ 0 \ -1]^T$).

Figure 4.21 shows the results from one subject. The two blue areas denoted by green ellipses on the figure are believed to be the activation due to the two flashing dots shown in one hemifield. When compared to the other figures, a clear indication exists that these two areas is connected by activation (area between the dots) in the other conditions. This furthermore provides a strong indication, that a back

projection from V5 (motion) is present and activates the not physically activated area in V1. The threshold is quite low, however, the two dots does not become connected in the FD condition despite of lowered threshold (parameter estimates are negative). Furthermore, the low threshold might in fact be reasonable according to Genovese et al. [34].

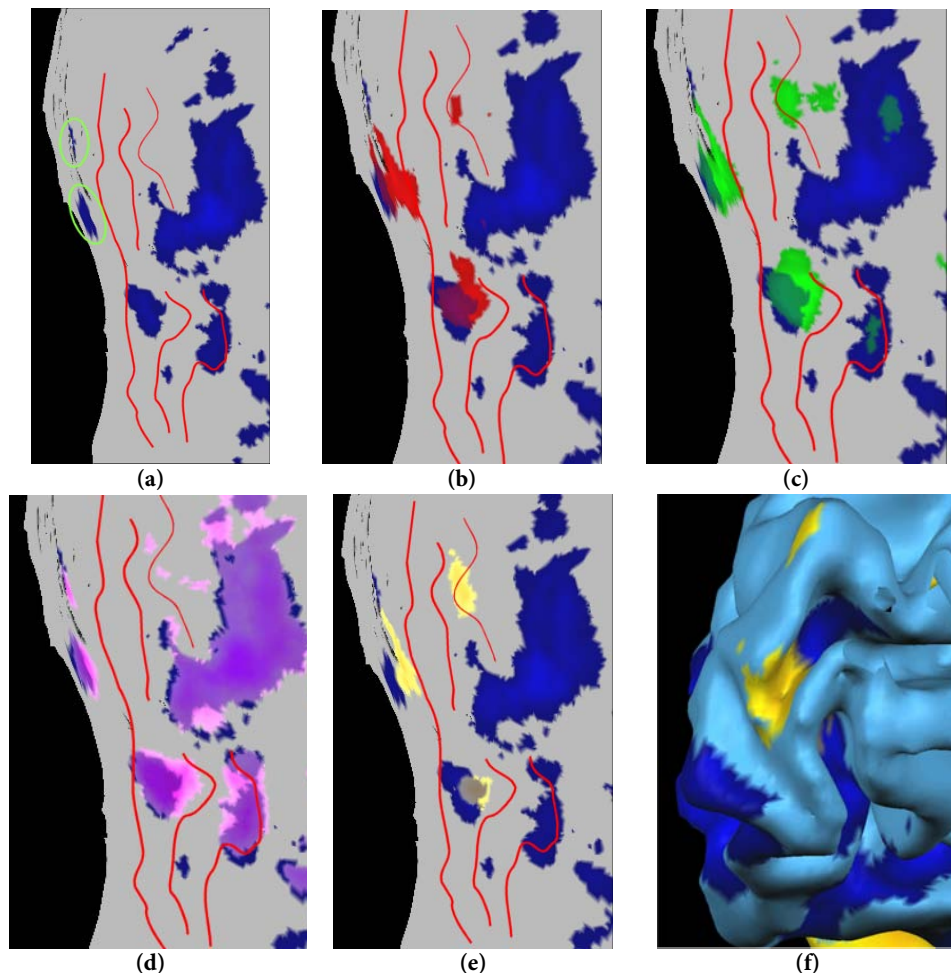


Figure 4.21: Results for V5-V1 back projection paradigm. Figure (a) shows the positive activation due to the FD condition (blue); this activation is shown in all figures from (a) to (e). In figure (a) the two green ellipses denote areas believed to represent the direct activation from the blinking dots. Figure (b) shows activation in the FB condition (red), figure (c) shows activation from RM condition (green), figure (d) shows activation in the AM condition (pink). Finally areas where activation due to the AM condition was greater than for the FD condition is shown in yellow in figure (e). Figure (f) shows the same as e for the left hemisphere however on a folded surface. The red lines in figures (a)-(e) are the borders between the first 3 visual areas found by the VFS computation. Voxels passing threshold of 0.20 (FDR) were considered active.

4.4 Other Results

4.4.1 Physiological Noise and Serial Correlation

The following section investigates the relation between serial autocorrelations in the residual time series and the inclusion of physiological parameters in the GLM used for analysis. The data used for this investigation is the time series from the V5-V1 back projection experiments described in section 4.3. This experiment was chosen because it consists of the largest number of time points and therefore allows for the best estimation of the 1st order AR (AR(1)) model coefficients.

First the GLM was fitted without the inclusion of physiological noise. The resulting AR(1) coefficients are presented in figure 4.22a. As already argued (see section 3.1.3) considerable positive autocorrelation is present. As expected after correction with the AR(1) model and a refit of the GLM, the estimated AR(1) coefficients are decreased considerably (see figure 4.22b). As physiological noise is temporally correlated, the inclusion of these confounds is expected to reduce residual autocorrelation. The result after inclusion of physiological noise is shown in figure 4.23.

The figure indicate that there might be a small advantage with respect to decreasing serial autocorrelations by doing correction for physiological noise, however the difference is only very small, therefore the colour map is scaled and the threshold is lowered.

Figure 4.23 therefore indicates that the effect on residual autocorrelation by inclusion of physiological parameters is only marginal (the effect on residual serial autocorrelation is negative in a considerable fraction of the voxels). This further indicates that the main course of serial autocorrelation is not physiological noise.

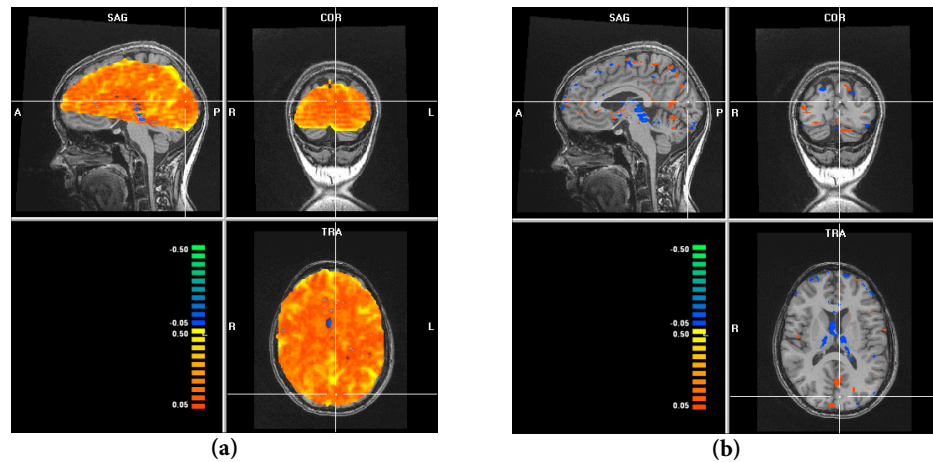


Figure 4.22: Estimated AR(1) model coefficients. Figure (a) shows the estimated coefficients ($\phi_{1,i}$) before correction by AR(1) model whereas (b) shows the same after correction.

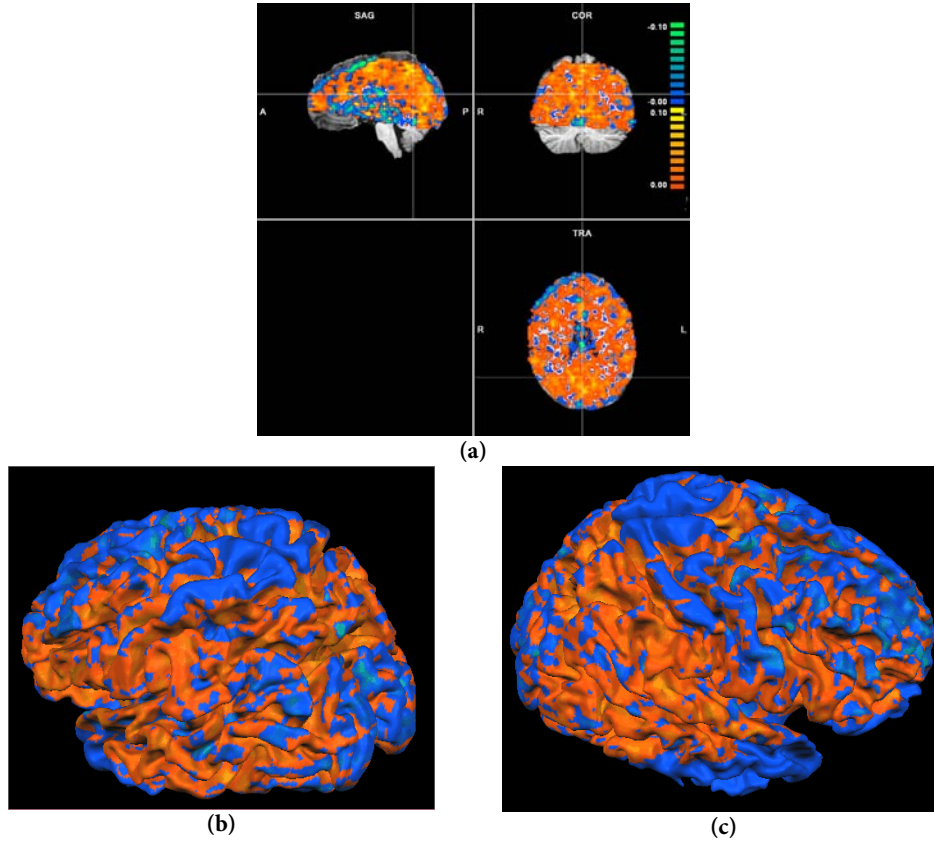


Figure 4.23: Difference in the AR(1) coefficients with and without modelling of physiological noise. Figure **a** shows a isometric view whereas (b) (view from the left side) and (c) (view of the right hemisphere) show the effect in cortical regions by overlaying the coefficients on the dilated and smoothed WM/GM surface. The values shown are the difference between the absolute value of the AR(1) model coefficients without correction for physiological noise and the same values using correction for physiological noise. That is: $\phi_d = |\phi_{1,i,\text{uncorrected}}| - |\phi_{1,i,\text{corrected}}|$. Blue/green regions denote regions where autocorrelation is increased by physiological noise in the GLM and red/yellow regions places where a decrease is observed. Figure a is thresholded at $|\phi_d| = 0.005$. It should be noted that figure (b) and (c) are not thresholded meaning that regions not covered by the functional scan or where the difference is zero are blue ($\phi_d=0$).

4.4.2 Retinotopic Mapping and Robustness

No explicit test for reproducibility has been implemented; however, the following results indicate that activation is in fact quite robust. The retinotopic mapping experiment was done on a patient suffering from epilepsy. Movement during the scanning session was so severe that the structural scan was useless for reconstruction of anatomical features. Still the results from the functional scan provide activation (see figure 4.24), even though the movement correction parameters revealed massive movement during the scan. This indicates that the activation is quite robust with respect to noise.

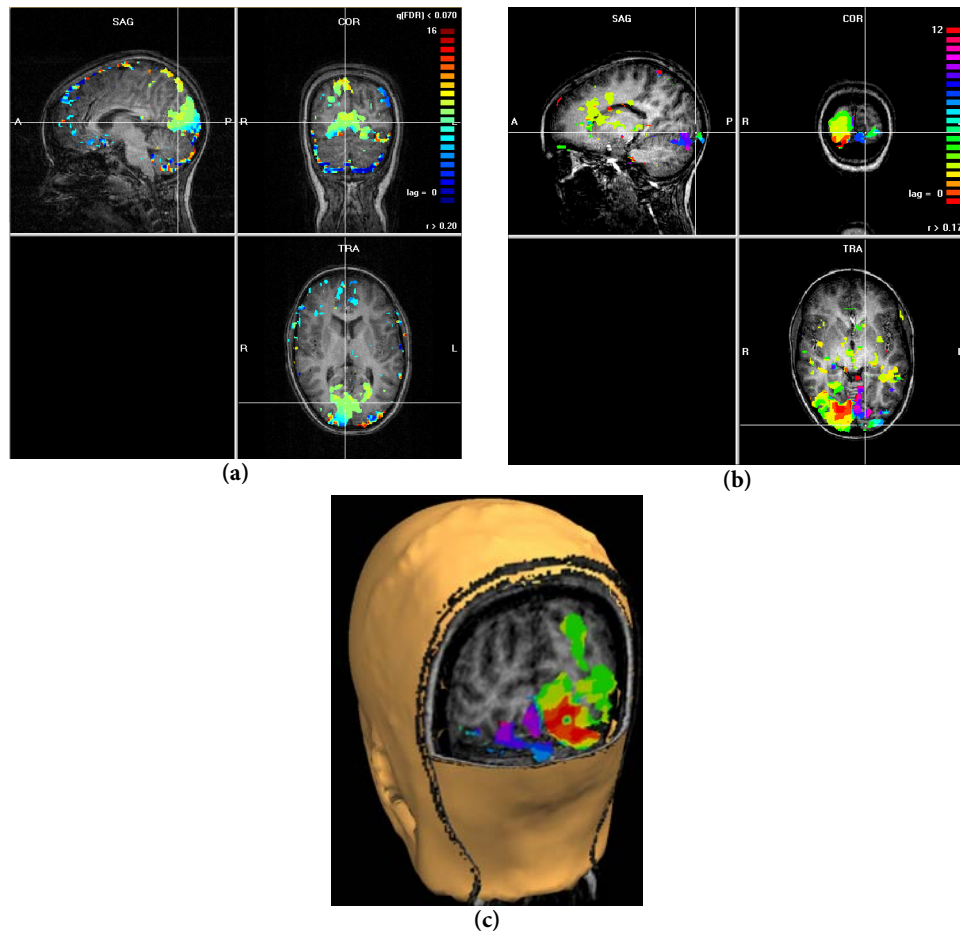


Figure 4.24: Robustness of the retinotopic mapping activation. Figure (a) shows the results from the eccentricity mapping experiment the activation threshold it set to $p=0.07$ (FDR). Movement related artefacts are visible at the edges of the brain. Figure (b) shows the same for the polar mapping experiment here the threshold is selected at $p=0.05$ (FDR) also here problems related to noise (activation elsewhere than the visual cortex) is visible, the position indicated by the cross is the approximate location of a tumour (activity is seen to be absent in this region). Figure (c) shows the activation from figure (b) in a sliced version of the reconstructed surface of the head. Note that the quality of the structural scan is quite low (noise due to movement) and anatomical features are hardly visible. The structural scan did not have quality sufficient for segmentation.

5 Discussion

The work with different software packages have been challenging especially in cases where functions were not working as expected or not yet implemented. This occurred several times with the recently released (May 2004) BrainVoyager QX 1.0 which has been used extensively (in pre-release versions) during the project. When problems occurred the choice was to either write the appropriate routines or use other software packages (both of which have been done in the project).

Before using any methods clinically, reproducibility of the results have to be proven. In this study this issue has not been addressed thoroughly, mostly due to the time limitations. However, although the methods described in this thesis have not been fully tested they provide a set of tools useful for investigating the visual cortex. Long term applications include pre-surgical planning and scientific studies of the brain. In this context a study using the retinotopic mapping described in section 4.1 have been planned aiming to investigate vision in patients suffering from Optic Neuritis⁴⁵.

Although very preliminary and not examined on sufficient subjects to make conclusions, the perimetry study performed has interesting perspectives for investigations on clinically relevant patients.

The preliminary results obtained with the V5-V1 back projection paradigm strongly indicated the presence of V5-V1 back projection. This issue has been extensively investigated by others and is still an unanswered question [62]. The results obtained in this study are, although only preliminary, interesting and hopefully helpful in unraveling the questions of V5-V1 back projection.

In the experiment concerning stereo vision the results showed that activation was seen mostly in secondary visual areas believed to be V3 and V5. This is in accordance with assumptions that the stereoscopic pathways include additional processing beyond V1 and that neurons in V3 may play a special role in the stereo pathway [1,4]. In addition to V3 the results in this study showed activation widespread in the extrastriate cortex, also consistent with previous findings[4].

The hemodynamic lag found in this study showed conflicting results when comparing with other findings [35]. This indicates that another HRF might be appro-

⁴⁵ Degeneration of the myelin sheet surrounding the optic nerve believed to be an onset symptom of Multiple Sclerosis[77].

prate in the visual cortex. Although a difference of 1 s may not influence the findings of activation, a possibility exist, that activation could be lost due to inadequate HRF timing. This should however be subjected to further investigations before any conclusive statements are made.

The functional mapping of the visual cortex produced results comparable to the literature [17,20,21,68,69,95] and consistency of the activation between all subjects scanned⁴⁶ was seen. This indicates that the paradigm and the GLM used for analysis are sufficient and no adjustments are required in order to obtain reliable results. Other experiments could therefore be interesting using other imaging methods, having less detection power but expected to have better localization such as EPI spin echo or arterial spin labelling⁴⁷ instead of EPI GE used in these studies [6,58,96].

Even though the activation is seen to be quite robust, the assignments of the activity to the cortical surface could be improved in relation to both the quality and automation.

A possible large cofounder in assigning activation data to the reconstructed surface is misalignment between the functional and the structural scan. Even though the positioning from the scanner was saved, fine adjustment was needed. The maximum likelihood method implemented in SPM2 [26] or BrainVoyager usually did not provide satisfactory results and manual editing was necessary. The functional scan did not provide full brain coverage, adding more slices might improve the automatic co-registration. Another more severe reason for misalignment might be distortions in the EPI images, systematic spatial distortion in EPI images have been reported by Wald et al. [94]. Furthermore retinotopic mapping studies in the literature is usually performed at 1.5 T [20,69,71,75,98] and distortions are known to be more severe at higher field strengths. In addition, some authors [98] have used special sequences or compromised the timing parameters to obtain distortion free EPI images.

A method for doing retinotopic mapping using a volumetric approach has been suggested by Dumoulin et al. [18]. This method should be sufficient to create regions of interest according to the visual areas. The advantage of this method is that an accurate segmentation into grey and white matter is not necessary.

Because the estimation of the Jacobian and thereby the delimitation of the borders between the visual area is extremely vulnerable to noise in the phase maps another approach might be considered. The two radial and the polar phase maps could be normalized to a template by the use of a statistical shape model. This method has been pursued by Dougherty et al. [17].

⁴⁶ 10 subjects have been scanned using the same stimulus for retinotopic mapping all these produced consistent results, however due to time limitation only 3 have been analyzed using surface based analysis.

⁴⁷ One preliminary result has already been done however results did not shown activation – more research is being done.

In fMRI there is strong tradition for doing multi subject analysis; this is, however, not a standard procedure for surface based studies. This is related to the fact that there might be large anatomical differences between subjects. A method to align surface maps has been suggested by Fischl et al. [24]. This method involves inflating each hemisphere to a sphere. The spheres from different subjects are then aligned (rotation) to obtain a matching structure (based on the curvature from the original folded surface model). This technique could be adopted to use the delimited borders of the visual areas for alignment. This might reduce variability between subjects considerable as quite large differences in the visual areas have been reported [17].

The experiments addressed in this study are as previously stated quite noise vulnerable. Because the methods used in this study did not exhibit sufficient sensitivity in regards to noise other methods like ICA or PCA was considered. However, due to time limitations this has not yet been implemented. One way to perform this implementation would be to use every four voxels or so in search for global variations in the time series thereby identifying common components for the entire brain (such as physiological noise and movement). By filtering the data with the components found, noise could potentially be reduced considerable. This however remains to be established and further investigations on the topic are needed.

By including physiological parameters in the analysis it is possible to disregard activation due to these confounders. In addition, it is expected to reduce residual autocorrelation. In this study no reliable results were obtained concerning this issue and further investigations are needed in order to draw final conclusions. However, the results did indicate that the main reason for serial autocorrelations is not physiological noise. Because the results are obtained using only the standard method implemented in BrainVoyager one way to further investigate this issue could be the use of other methods to estimate AR model coefficients. Furthermore, the effects of adding higher order AR models could be investigated. In addition, the effect on residual serial autocorrelations by performing noise filtering by ICA.

Conclusion

The method used for segmentation, inflation and unfolding of the cortex based on the structural images proved efficient for reconstructing the cortical grey matter surface and for overlaying activity found in the analysis of the functional images.

This study used a GLM for analysis of functional mapping of the visual cortex. The methods used proved robust related to sensitivity and noise. By comparing the result obtained in the retinotopic mapping experiment to an ICA of the data it was found that 2 harmonics were enough to describe the dynamics of the BOLD response. An estimation of the hemodynamic lag was performed and a value of approximately 4.2 s (time to peak) was observed. Delimitation of the borders of the visual areas was performed, however, the method was not able to provide conclusive results in all subjects. This problem was probably related to misalignment between the structural and the functional images.

The presence of a V5-V1 back projection was strongly indicated by the result obtained in the V5-V1 back projection paradigm, and further investigations of this topic is ongoing. In addition the retinotopic mapping described has been planned for clinically investigations of patients with Optic Neuritis.

The proposed stereo vision stimuli showed a possible activation of V5, V3 and other secondary visual areas in response to the colour coded 3-D images displayed.

Furthermore, the investigation of physiological noise parameters provided indication that physiological noise is not one of the main causes of residual autocorrelation in fMRI data.

Bibliography

- [1] Adams DL, Zeki S. Functional organization of macaque V3 for stereoscopic depth. *J Neurophysiol.* 2001;86:2195-2203.
- [2] Aguirre GK, Zarahn E, D'Esposito M. Empirical analyses of BOLD fMRI statistics. II. Spatially smoothed data collected under null-hypothesis and experimental conditions. *Neuroimage.* 1997;5(3):199-212.
- [3] Aine CJ, Supek S, George JS et al. Retinotopic organization of human visual cortex: departures from the classical model. *Cereb Cortex.* 1996;6(3):354-361.
- [4] Backus BT, Fleet DJ, Parker AJ, Heeger DJ. Human cortical activity correlates with stereoscopic depth perception. *J Neurophysiol.* 2001;86:2054-2068.
- [5] Bandettini PA, Jesmanowicz A, Wong EC, Hyde JS. Processing strategies for time-course data sets in functional MRI of the human brain. *Magn Reson Med.* 1993;30(2):161-173.
- [6] Bandettini PA, Wong EC, Jesmanowicz A et al. Spin-echo and gradient-echo EPI of human brain activation using BOLD contrast: a comparative study at 1.5 T. *NMR Biomed.* 1994;7:12-20.
- [7] Beer J, Blakemore C, Previc FH, Liotti M. Areas of the human brain activated by ambient visual motion, indicating three kinds of self-movement. *Exp Brain Res.* 2002;143(1):78-88.
- [8] Boynton GM, Engel SA, Glover GH, Heeger DJ. Linear systems analysis of functional magnetic resonance imaging in human V1. *J Neurosci.* 1996;16(13):4207-4221.
- [9] Buxton RB, Wong EC, Frank LR. Dynamics of blood flow and oxygenation changes during brain activation: the balloon model. *Magn Reson Med.* 1998;39:855-864.
- [10] Buxton RB. Introduction to functional magnetic resonance imaging: principles & techniques. Cambridge University Press, 2002.

- [11] Calhoun VD, Adali T, Pearlson GD, Pekar JJ. Spatial and temporal independent component analysis of functional MRI data containing a pair of task-related waveforms. *Hum Brain Mapp.* 2001;13(1):43-53.
- [12] Dagli MS, Ingelholm JE, Haxby JV. Localization of cardiac-induced signal change in fMRI. *Neuroimage.* 1999;9:407-415.
- [13] Dale AM, Fischl B, Sereno MI. Cortical surface-based analysis. I. Segmentation and surface reconstruction. *Neuroimage.* 1999;9:179-194.
- [14] Deiber MP, Ibanez V, Honda M et al. Cerebral processes related to visuomotor imagery and generation of simple finger movements studied with positron emission tomography. *Neuroimage.* 1998;7(2):73-85.
- [15] DeYoe EA, Bandettini P, Neitz J et al. Functional magnetic resonance imaging (fMRI) of the human brain. *J Neurosci Methods.* 1994;54(2):171-187.
- [16] DeYoe EA, Carman GJ, Bandettini P et al. Mapping striate and extrastriate visual areas in human cerebral cortex. *Proc Natl Acad Sci U S A.* 1996;93:2382-2386.
- [17] Dougherty RF, Koch VM, Brewer AA et al. Visual field representations and locations of visual areas V1/2/3 in human visual cortex. *J Vis.* 2003;3:586-598.
- [18] Dumoulin SO, Hoge RD, Baker CLJ et al. Automatic volumetric segmentation of human visual retinotopic cortex. *Neuroimage.* 2003;18:576-587.
- [19] Duncan RO, Boynton GM. Cortical magnification within human primary visual cortex correlates with acuity thresholds. *Neuron.* 2003;38:659-671.
- [20] Engel SA, Glover GH, Wandell BA. Retinotopic organization in human visual cortex and the spatial precision of functional MRI. *Cereb Cortex.* 1997;7:181-192.
- [21] Engel SA, Rumelhart DE, Wandell BA et al. fMRI of human visual cortex. *Nature.* 1994;369:525.
- [22] Esposito F, Formisano E, Seifritz E et al. Spatial independent component analysis of functional MRI time-series: to what extent do results depend on the algorithm used? *Hum Brain Mapp.* 2002;16:146-157.
- [23] Fawcett IP, Barnes GR, Hillebrand A, Singh KD. The temporal frequency tuning of human visual cortex investigated using synthetic aperture magnetometry. *Neuroimage.* 2004;21(4):1542-1553.
- [24] Fischl B, Sereno MI, Dale AM. Cortical surface-based analysis. II: Inflation, flattening, and a surface-based coordinate system. *Neuroimage.* 1999;9:195-207.
- [25] Frackowiak RS, Friston KJ, Frith CD et al. Human Brain Function. Academic Press USA, 1997.

- [26] Friston KJ, Ashburner J, Poline J et al. Spatial registration and normalisation of images. *Hum Brain Mapp.* 1995;(2):165-189.
- [27] Friston KJ, Buchel C. Attentional modulation of effective connectivity from V2 to V5/MT in humans. *Proc Natl Acad Sci U S A.* 2000;97:7591-7596.
- [28] Friston KJ, Frith CD, Liddle PF et al. The relationship between global and local changes in PET scans. *J Cereb Blood Flow Metab.* 1990;10:458-466.
- [29] Friston KJ, Holmes AP, Poline JB et al. Analysis of fMRI time-series revisited. *Neuroimage.* 1995;2:45-53.
- [30] Friston KJ, Holmes AP, Worsley KJ et al. Statistical Parametric maps in functional imaging: A general linear approach. *Hum Brain Mapp.* 1995;2:189-210.
- [31] Friston KJ, Josephs O, Zarahn E et al. To smooth or not to smooth? Bias and efficiency in fMRI time-series analysis. *Neuroimage.* 2000;12:196-208.
- [32] Friston KJ, Mechelli A, Turner R, Price CJ. Nonlinear responses in fMRI: the Balloon model, Volterra kernels, and other hemodynamics. *Neuroimage.* 2000;12:466-477.
- [33] Friston KJ, Williams S, Howard R et al. Movement-related effects in fMRI time-series. *Magn Reson Med.* 1996;35:346-355.
- [34] Genovese CR, Lazar NA, Nichols T. Thresholding of statistical maps in functional neuroimaging using the false discovery rate. *Neuroimage.* 2002;15(4):870-878.
- [35] Gössl C, Fahrmeir L, Auer DP. Bayesian Modeling of the Hemodynamic Response Function in BOLD fMRI. *Neuroimage.* 2001;14:140-148.
- [36] Gudbjartsson H, Patz S. The Rician distribution of noisy MRI data. *Magn Reson Med.* 1995;34(6):910-914.
- [37] Guye M, Parker GJ, Symms M et al. Combined functional MRI and tractography to demonstrate the connectivity of the human primary motor cortex in vivo. *Neuroimage.* 2003;19(4):1349-1360.
- [38] Halgren E, Dale AM, Sereno MI et al. Location of human face-selective cortex with respect to retinotopic areas. *Hum Brain Mapp.* 1999;7:29-37.
- [39] Hansen PS. Colour Encoding for Stereoscopic Displays in Virtual Construction Environments. *Proc of the 1st Intl Conf on Advanced Research in Virtual and Rapid Prototyping.* 2003;329-333.
- [40] Hood DC, Odel JG, Winn BJ. The multifocal visual evoked potential. *J Neuroophthalmol.* 2003;23(4):279-289.
- [41] Hubel D. Eye, Brain, and Vision. Scientific American Library, 1995.

- [42] Huk AC, Dougherty RF, Heeger DJ. Retinotopy and functional subdivision of human areas MT and MST. *J Neurosci.* 2002;22:7195-7205.
- [43] Hyvarinen A. Fast and robust fixed-point algorithms for independent component analysis. *IEEE Trans Neural Netw.* 1999;10:626-634.
- [44] Kastrup A, Kruger G, Glover GH et al. Regional variability of cerebral blood oxygenation response to hypercapnia. *Neuroimage.* 1999;10(6):675-681.
- [45] Kim DS, Duong TQ, Kim SG. High-resolution mapping of iso-orientation columns by fMRI. *Nat Neurosci.* 2000;3(2):164-169.
- [46] Kriegeskorte N, Goebel R. An efficient algorithm for topologically correct segmentation of the cortical sheet in anatomical mr volumes. *Neuroimage.* 2001;14:329-346.
- [47] Kwong KK, Belliveau JW, Chesler DA et al. Dynamic magnetic resonance imaging of human brain activity during primary sensory stimulation. *Proc Natl Acad Sci U S A.* 1992;89(12):5675-5679.
- [48] Lancaster J, Summerlin J, RL et al. The Talairach Daemon, a database server for Talairach Atlas Labels. *Neuroimage.* 1997;5(4):S633.
- [49] Lee JS. Digital image smoothing and the sigma filter. *Vis Graph Image Process.* 1983;24:255-269.
- [50] Lund, T. E. GLM approach for correction of physiological noise in fMRI data. 2003. Personal Communication
- [51] Marple SL. Chapter 7. Digital Spectral Analysis. 1987.
- [52] McKeown MJ, Hansen LK, Sejnowski TJ. Independent component analysis of functional MRI: what is signal and what is noise? *Curr Opin Neurobiol.* 2003;13:620-629.
- [53] McKeown MJ, Jung T-P, Makeig S et al. Spatially independent activity patterns in functional MRI data during the Stroop color-naming task. *Proc Natl Acad Sci U S A.* 1998;95(3):803-810.
- [54] McKeown MJ, Makeig S, Brown G et al. Analysis of fMRI Data by Blind Separation Into Independent Spatial Components. *Hum Brain Mapp.* 1998;6:160-188.
- [55] McKeown MJ, Sejnowski TJ. Independent Component Analysis of fMRI Data: Examining the Assumptions. *Hum Brain Mapp.* 1998;6:368-372.
- [56] Morland AB, Baseler HA, Hoffmann MB et al. Abnormal retinotopic representations in human visual cortex revealed by fMRI. *Acta Psychol (Amst).* 2001;107(1-3):229-247.

- [57] Nichols T, Hayasaka S. Controlling the familywise error rate in functional neuroimaging: a comparative review. *Stat Methods Med Res.* 2003;12(5):419-446.
- [58] Norris DG, Zysset S, Mildner T, Wiggins CJ. An investigation of the value of spin-echo-based fMRI using a Stroop color-word matching task and EPI at 3 T. *Neuroimage.* 2002;15:719-726.
- [59] Ogawa S, Lee TM, Kay AR, Tank DW. Brain magnetic resonance imaging with contrast dependent on blood oxygenation. *Proc Natl Acad Sci U S A.* 1990;87:9868-9872.
- [60] Ogawa S, Lee TM, Nayak AS, Glynn P. Oxygenation-sensitive contrast in magnetic resonance image of rodent brain at high magnetic fields. *Magn Reson Med.* 1990;14:68-78.
- [61] Ogawa S, Tank DW, Menon R et al. Intrinsic signal changes accompanying sensory stimulation: functional brain mapping with magnetic resonance imaging. *Proc Natl Acad Sci U S A.* 1992;89:5951-5955.
- [62] Pascual-Leone A, Walsh V. Fast backprojections from the motion to the primary visual area necessary for visual awareness. *Science.* 2001;292(5516):510-512.
- [63] Popovic Z, Sjostrand J. Resolution, separation of retinal ganglion cells, and cortical magnification in humans. *Vision Res.* 2001;41:1313-1319.
- [64] Reppas JB, Niyogi S, Dale AM et al. Representation of motion boundaries in retinotopic human visual cortical areas. *Nature.* 1997;388:175-179.
- [65] Rosenzweig MR, Breedlove SM, Watson NV. Vision: From Eye to Brain. Biological Psychology, An Introduction to Cognitive and Behavioral Neuroscience. Sinauer Associates, 2004.
- [66] Schmitt F, Stehling MK, Turner R. Echo-planar imaging: theory, technique, and application. Springer, 1998.
- [67] Schwartz EL. A quantitative model of the functional architecture of human striate cortex with application to visual illusion and cortical texture analysis. *Biol Cybern.* 1980;37(2):63-76.
- [68] Sereno MI, Dale AM, Reppas JB et al. Borders of multiple visual areas in humans revealed by functional magnetic resonance imaging. *Science.* 1995;268:889-893.
- [69] Sereno MI, McDonald CT, Allman JM. Analysis of retinotopic maps in extrastriate cortex. *Cereb Cortex.* 1994;4(6):601-620.
- [70] Sereno MI, Pitzalis S, Martinez A. Mapping of contralateral space in retinotopic coordinates by a parietal cortical area in humans. *Science.* 2001;294:1350-1354.

- [71] Shipp S, Watson JD, Frackowiak RS, Zeki S. Retinotopic maps in human prestriate visual cortex: the demarcation of areas V2 and V3. *Neuroimage*. 1995;2(2):125-132.
- [72] Slotnick SD, Klein SA, Carney T, Sutter EE. Electrophysiological estimate of human cortical magnification. *Clin Neurophysiol*. 2001;112:1349-1356.
- [73] Slotnick SD, Moo LR. Retinotopic mapping reveals extrastriate cortical basis of homonymous quadrantanopia. *Neuroreport*. 2003;14(9):1209-1213.
- [74] Slotnick SD, Moo LR, Krauss G, Hart J, Jr. Large-scale cortical displacement of a human retinotopic map. *Neuroreport*. 2002;13(1):41-46.
- [75] Slotnick SD, Yantis S. Efficient acquisition of human retinotopic maps. *Hum Brain Mapp*. 2003;18:22-29.
- [76] Smith AM, Lewis BK, Ruttimann UE et al. Investigation of low frequency drift in fMRI signal. *Neuroimage*. 1999;9(5):526-533.
- [77] Sorensen TL, Frederiksen JL, Bronnum-Hansen H, Petersen HC. Optic neuritis as onset manifestation of multiple sclerosis: a nationwide, long-term survey. *Neurology*. 1999;53(3):473-478.
- [78] Talairach J, Tournoux P. Co-planar stereotaxic atlas of the human brain. Thieme, New York, 1988.
- [79] Thesen S, Heid O, Mueller E, Schad LR. Prospective acquisition correction for head motion with image-based tracking for real-time fMRI. *Magn Reson Med*. 2000;44:457-465.
- [80] Tootell RB, Dale AM, Sereno MI, Malach R. New images from human visual cortex. *Trends Neurosci*. 1996;19(11):481-489.
- [81] Tootell RB, Hadjikhani N. Where is 'dorsal V4' in human visual cortex? Retinotopic, topographic and functional evidence. *Cereb Cortex*. 2001;11:298-311.
- [82] Tootell RB, Hadjikhani NK, Vanduffel W et al. Functional analysis of primary visual cortex (V1) in humans. *Proc Natl Acad Sci U S A*. 1998;95:811-817.
- [83] Tootell RB, Mendola JD, Hadjikhani NK et al. Functional analysis of V3A and related areas in human visual cortex. *J Neurosci*. 1997;17:7060-7078.
- [84] Tootell RB, Nelissen K, Vanduffel W, Orban GA. Search for color 'center(s)' in macaque visual cortex. *Cereb Cortex*. 2004;14(4):353-363.
- [85] Tootell RB, Reppas JB, Dale AM et al. Visual motion aftereffect in human cortical area MT revealed by functional magnetic resonance imaging. *Nature*. 1995;375:139-141.

- [86] Tootell RB, Silverman MS, Switkes E, De Valois RL. Deoxyglucose analysis of retinotopic organization in primate striate cortex. *Science*. 1982;218:902-904.
- [87] Tootell RB, Switkes E, Silverman MS, Hamilton SL. Functional anatomy of macaque striate cortex. II. Retinotopic organization. *J Neurosci*. 1988;8(5):1531-1568.
- [88] Tootell RB, Tsao D, Vanduffel W. Neuroimaging weighs in: humans meet macaques in "primate" visual cortex. *J Neurosci*. 2003;23(10):3981-3989.
- [89] Turner R, Howseman A, Rees GE et al. Functional magnetic resonance imaging of the human brain: data acquisition and analysis. *Exp Brain Res*. 1998;123:5-12.
- [90] Van Essen DC, Drury HA. Structural and functional analyses of human cerebral cortex using a surface-based atlas. *J Neurosci*. 1997;17:7079-7102.
- [91] Van Essen DC, Lewis JW, Drury HA et al. Mapping visual cortex in monkeys and humans using surface-based atlases. *Vision Res*. 2001;41:1359-1378.
- [92] Vaughan JT, Garwood M, Collins CM et al. 7T vs. 4T: RF power, homogeneity, and signal-to-noise comparison in head images. *Magn Reson Med*. 2001;46:24-30.
- [93] Virsu V, Hari R. Cortical magnification, scale invariance and visual ecology. *Vision Res*. 1996;36:2971-2977.
- [94] Wald L, Schmitt F, Dale AM. Systematic spatial distortion in MRI due to gradient non-linearities. *Neuroimage (Proc of HBM 2001)*. 2001;13(6):S50.
- [95] Wandell BA. Computational neuroimaging of human visual cortex. *Annu Rev Neurosci*. 1999;22:145-173.
- [96] Wang J, Aguirre GK, Kimberg DY et al. Arterial spin labeling perfusion fMRI with very low task frequency. *Magn Reson Med*. 2003;49(5):796-802.
- [97] Wansapura JP, Holland SK, Dunn RS, Ball WS, Jr. NMR relaxation times in the human brain at 3.0 tesla. *J Magn Reson Imaging*. 1999;9(4):531-538.
- [98] Warnking J, Dojat M, Guerin-Dugue A et al. fMRI retinotopic mapping--step by step. *Neuroimage*. 2002;17:1665-1683.
- [99] Woolrich MW, Ripley BD, Brady M, Smith SM. Temporal Autocorrelation in Univariate Linear Modeling of FMRI Data. *Neuroimage*. 2001;14:1370-1386.

-
- [100] Worsley KJ, Friston KJ. Analysis of fMRI time-series revisited--again. *Neuroimage*. 1995;2:173-181.
 - [101] Worsley KJ, Liao CH, Aston J et al. A general statistical analysis for fMRI data. *Neuroimage*. 2002;15(1):1-15.
 - [102] Zarahn E, Aguirre GK, D'Esposito M. Empirical analyses of BOLD fMRI statistics. I. Spatially unsmoothed data collected under null-hypothesis conditions. *Neuroimage*. 1997;5(3):179-197.
 - [103] Zeki S. A Vision of the Brain. Blackwell Scientific Publications, 1993.